



# ALMA [C I]<sup>3</sup>P<sub>1</sub>–<sup>3</sup>P<sub>0</sub> Observations of NGC 6240: A Puzzling Molecular Outflow, and the Role of Outflows in the Global $\alpha_{\text{CO}}$ Factor of (U)LIRGs

Claudia Cicone<sup>1,15</sup>, Paola Severgnini<sup>1</sup>, Padelis P. Papadopoulos<sup>2,3,4</sup>, Roberto Maiolino<sup>5,6</sup>, Chiara Feruglio<sup>7</sup>, Ezequiel Treister<sup>8</sup>, George C. Privon<sup>9</sup>, Zhi-yu Zhang<sup>10,11</sup>, Roberto Della Ceca<sup>1</sup>, Fabrizio Fiore<sup>12</sup>, Kevin Schawinski<sup>13</sup>, and Jeff Wagg<sup>14</sup>

<sup>1</sup> INAF—Osservatorio Astronomico di Brera, Via Brera 28, I-20121 Milano, Italy; [claudia.cicone@brera.inaf.it](mailto:claudia.cicone@brera.inaf.it)

<sup>2</sup> Department of Physics, Section of Astrophysics, Astronomy and Mechanics, Aristotle University of Thessaloniki, Thessaloniki, Macedonia, 54124, Greece

<sup>3</sup> Research Center for Astronomy, Academy of Athens, Soranou Efessiou 4, GR-115 27 Athens, Greece

<sup>4</sup> School of Physics and Astronomy, Cardiff University, Queen’s Buildings, The Parade, Cardiff, CF24 3AA, UK

<sup>5</sup> Cavendish Laboratory, University of Cambridge, 19 J. J. Thomson Ave., Cambridge CB3 0HE, UK

<sup>6</sup> Kavli Institute of Cosmology Cambridge, Madingley Road, Cambridge CB3 0HA, UK

<sup>7</sup> INAF—Osservatorio Astronomico di Trieste, via G.B. Tiepolo 11, I-34143 Trieste, Italy

<sup>8</sup> Instituto de Astrofísica, Facultad de Física, Pontificia Universidad Católica de Chile, Casilla 306, Santiago 22, Chile

<sup>9</sup> Department of Astronomy, University of Florida, 211 Bryant Space Sciences Center, Gainesville, 32611 FL, USA

<sup>10</sup> European Southern Observatory, Karl-Schwarzschild-Str. 2, D-85748 Garching, Germany

<sup>11</sup> Institute for Astronomy, University of Edinburgh, Royal Observatory, Blackford Hill, Edinburgh EH9 3HJ, UK

<sup>12</sup> INAF—Osservatorio Astronomico di Roma, via Frascati 33, I-00078 Monteporzio Catone, Italy

<sup>13</sup> Institute for Particle Physics and Astrophysics, ETH Zurich, Wolfgang-Pauli-Str. 27, CH-8093 Zurich, Switzerland

<sup>14</sup> SKA Organisation, Lower Withington Macclesfield, Cheshire SK11 9DL, UK

Received 2018 April 7; revised 2018 June 29; accepted 2018 July 11; published 2018 August 20

## Abstract

We present Atacama large millimeter/submillimeter array (ALMA) and compact array (ACA) [C I]<sup>3</sup>P<sub>1</sub>–<sup>3</sup>P<sub>0</sub> ([C I](1–0)) observations of NGC 6240, which we combine with ALMA CO(2–1) and IRAM Plateau de Bure Interferometer CO(1–0) data to study the physical properties of the massive molecular (H<sub>2</sub>) outflow. We discover that the receding and approaching sides of the H<sub>2</sub> outflow, aligned east–west, exceed 10 kpc in their total extent. High resolution (0″.24) [C I](1–0) line images surprisingly reveal that the outflow emission peaks *between* the two active galactic nuclei (AGNs), rather than on either of the two, and that it dominates the velocity field in this nuclear region. We combine the [C I](1–0) and CO(1–0) data to constrain the CO-to-H<sub>2</sub> conversion factor ( $\alpha_{\text{CO}}$ ) in the outflow, which is on average  $2.1 \pm 1.2 M_{\odot} (\text{K km s}^{-1} \text{ pc}^2)^{-1}$ . We estimate that  $60 \pm 20\%$  of the total H<sub>2</sub> gas reservoir of NGC 6240 is entrained in the outflow, for a resulting mass-loss rate of  $\dot{M}_{\text{out}} = 2500 \pm 1200 M_{\odot} \text{ yr}^{-1} \equiv 50 \pm 30 \text{ SFR}$ . These energetics rule out a solely star formation-driven wind, but the puzzling morphology challenges a classic radiative-mode AGN feedback scenario. For the quiescent gas, we compute  $\langle \alpha_{\text{CO}} \rangle = 3.2 \pm 1.8 M_{\odot} (\text{K km s}^{-1} \text{ pc}^2)^{-1}$ , which is at least twice the value commonly employed for (ultra) luminous infrared galaxies (U)LIRGs. We observe a tentative trend of increasing  $r_{21} \equiv L'_{\text{CO}(2-1)} / L'_{\text{CO}(1-0)}$  ratios with velocity dispersion and measure  $r_{21} > 1$  in the outflow, whereas  $r_{21} \simeq 1$  in the quiescent gas. We propose that molecular outflows are the location of the warmer, strongly unbound phase that partially reduces the opacity of the CO lines in (U)LIRGs, hence driving down their global  $\alpha_{\text{CO}}$  and increasing their  $r_{21}$  values.

**Key words:** galaxies: active – galaxies: evolution – galaxies: individual (NGC 6240) – galaxies: ISM – submillimeter: ISM

## 1. Introduction

Massive ( $M_{\text{mol}} > 10^8 M_{\odot}$ ) and extended ( $r \gtrsim 1 \text{ kpc}$ ) outflows of cold and dense molecular (H<sub>2</sub>) gas have been discovered in a large number of starbursts and active galactic nuclei (AGNs) (Turner 1985; Nakai et al. 1987; Sakamoto et al. 2006; Feruglio et al. 2010, 2013a, 2017; Fischer et al. 2010; Alatalo et al. 2011; Sturm et al. 2011; Dasyra & Combes 2012; Combes et al. 2013; Morganti et al. 2013; Spoon et al. 2013; Veilleux et al. 2013; Cicone et al. 2014; García-Burillo et al. 2014, 2015; Zschaechner et al. 2016; Carniani et al. 2017; Barcos-Muñoz et al. 2018; Fluetsch et al. 2018; Gowardhan et al. 2018). Although so far limited mostly to local (ultra) luminous infrared galaxies ([U]LIRGs), these observations indicate that the mass-loss rates of H<sub>2</sub> gas are higher compared to the ionized gas phase participating in the outflows (Carniani et al. 2015; Fiore et al. 2017). Therefore, molecular outflows, by displacing and perhaps removing the fuel available for star formation, can have a

strong impact on galaxy evolution. More luminous AGNs host more powerful H<sub>2</sub> winds, suggesting a direct link between the two (Cicone et al. 2014).

The presence of massive amounts of cold and dense H<sub>2</sub> gas outflowing at  $v \gtrsim 1000 \text{ km s}^{-1}$  across kpc scales in galaxies is itself puzzling. A significant theoretical effort has gone into reproducing the properties of multiphase outflows in the context of AGN feedback models (Cicone et al. 2018). In one of the AGN radiative-mode scenarios, the outflows result from the interaction of fast highly ionized winds launched from the pc-scales with the kpc-scale interstellar medium (ISM), which occurs through a “blast-wave” mechanism (Silk & Rees 1998; King 2010; Faucher-Giguère & Quataert 2012; Zubovas & King 2012; Costa et al. 2014; Gaspari & Sądowski 2017; Biernacki & Teyssier 2018). In this picture, because molecular clouds overtaken by a hot and fast wind are quickly shredded (Brüggen & Scannapieco 2016), it is more likely that the high-velocity H<sub>2</sub> gas forms directly within the outflow, by cooling out of the warmer gas (Zubovas & King 2014; Costa et al. 2015; Nims et al. 2015;

<sup>15</sup> Marie Skłodowska-Curie fellow.

Thompson et al. 2016; Richings & Faucher-Giguère 2018). An alternative scenario, not requiring shockwaves, is the direct acceleration of the molecular ISM by radiation pressure on dust (Ishibashi & Fabian 2015; Thompson et al. 2015; Costa et al. 2018). This mechanism is most efficient in AGNs deeply embedded in a highly IR optically thick medium, such as local (U)LIRGs.

In order to advance our theoretical understanding of galactic-scale molecular outflows, we need to place more accurate constraints on their energetics. Indeed, most current  $H_2$  outflow mass estimates are based on a single molecular gas tracer (CO or OH), implying uncertainties of up to one order of magnitude (Veilleux et al. 2017; Cicone et al. 2018). The luminosity of the CO(1–0) line, which is optically thick in typical conditions of molecular clouds, can be converted into  $H_2$  mass through an CO(1–0)-to- $H_2$  conversion factor ( $\alpha_{CO}$ ) calibrated using known sources and dependent on the physical state of the gas. For the molecular ISM of isolated (or only slightly perturbed) disk galaxies like the Milky Way, the conventional  $\alpha_{CO}$  is  $4.3 M_\odot (K km s^{-1} pc^2)^{-1}$  (Bolatto et al. 2013). Instead, for merger-driven starbursts like most (U)LIRGs, which are characterized by a more turbulent and excited ISM, a lower  $\alpha_{CO}$  of  $\sim 0.6\text{--}1.0 M_\odot (K km s^{-1} pc^2)^{-1}$  is often adopted (Downes & Solomon 1998; Yao et al. 2003; Israel et al. 2015). Such low  $\alpha_{CO}$  values have been ascribed to the existence, in the inner regions of these mergers, of a warm and turbulent “envelope” phase of  $H_2$  gas, not contained in self-gravitating clouds (Aalto et al. 1995). However, some recent analyses of the CO spectral line energy distributions (SLEDs) including high- $J$  ( $\gtrsim 3$ ) transitions suggest that near-Galactic  $\alpha_{CO}$  values are also possible for (U)LIRGs, especially when a significant  $H_2$  gas fraction is in dense, gravitationally bound states (Papadopoulos et al. 2012a). Dust-based ISM mass measurements also deliver galactic-type  $\alpha_{CO}$  factors for (U)LIRGs, although they depend on the underlying assumptions used to calibrate the conversion (Scoville et al. 2016).

Molecular outflows can be significantly fainter than the quiescent ISM, and so multi-transition observations aimed at estimating their  $\alpha_{CO}$  are particularly challenging. Dasyra et al. (2016) and more recently Oosterloo et al. (2017), for the radio-jet driven outflow in IC 5063, derived a low optically thin  $\alpha_{CO}$  of  $\sim 0.3 M_\odot (K km s^{-1} pc^2)^{-1}$ , in line with theoretical predictions by Richings and Faucher-Giguère (2018). On the other hand, for the starburst-driven M82 outflow, Leroy et al. (2015) calculated<sup>16</sup>  $\alpha_{CO}^{2-1} = 1\text{--}2.5 M_\odot (K km s^{-1} pc^2)^{-1}$ . The detection of high density gas in the starburst-driven outflow of NGC 253 would also favor an  $\alpha_{CO}$  higher than the optically thin value (Walter et al. 2017), and a similar conclusion may be reached for the outflow in Mrk 231, found to entrain a substantial amount of dense  $H_2$  gas (Aalto et al. 2012, 2015; Cicone et al. 2012; Lindberg et al. 2016).

An alternative method for measuring the molecular gas mass, independent of the  $\alpha_{CO}$  factor, is through a tracer such as the  $^3P_1 - ^3P_0$  transition of neutral atomic carbon (hereafter [C I] (1–0)). This line, optically thin in most cases, has an easier partition function than molecules, and excitation requirements similar to CO(1–0).<sup>17</sup> More importantly, [C I] is expected

to be fully coexisting with  $H_2$  (Papadopoulos et al. 2004; Papadopoulos & Greve 2004). Therefore, by combining the information from CO(1–0) and [C I](1–0), it is possible to derive an estimate of the  $\alpha_{CO}$  value. Similar to any optically thin species used to trace  $H_2$  (e.g., dust,  $^{13}CO$ ), converting the [C I](1–0) line flux into a mass measurement is plagued by the unavoidable uncertainty on its abundance. However, in this regard, recent calculations found not only that the *average* [C/H<sub>2</sub>] abundance in molecular clouds is more robust than that of molecules such as CO, but also that [C I] can even trace the  $H_2$  gas where CO has been severely depleted by cosmic rays (CRs, Bisbas et al. 2015, 2017).

In this work we use new Atacama large millimeter/submillimeter array (ALMA) and Atacama compact array (ACA) observations of the [C I](1–0) line in NGC 6240 to constrain the physical properties of its molecular outflow. NGC 6240 is a merging LIRG hosting two AGNs with quasar-like luminosities (Puccetti et al. 2016). The presence of a molecular outflow was suggested by van der Werf et al. (1993), based on the detection of high-velocity wings of the ro-vibrational  $H_2$   $v = 1\text{--}0$  S(1)  $2.12 \mu m$  line and by Iono et al. (2007) based on the CO(3–2) kinematics, and it was later confirmed by Feruglio et al. (2013a) using IRAM PdBI CO (1–0) observations. This is one of the first interferometric [C I](1–0) observations of a local galaxy (see also Krips et al. 2016) and, to our knowledge, the first spatially resolved [C I](1–0) observation of a molecular outflow in a quasar. Probing the capability of [C I](1–0) to image molecular outflows is crucial: besides being an alternative  $H_2$  tracer independent of the  $\alpha_{CO}$  factor, [C I](1–0) is also sensitive to CO-poor gas, which may be an important component of molecular outflows exposed to strong far-ultraviolet (UV) fields (Wolfire et al. 2010) or CR fluxes (Bisbas et al. 2015, 2017; Krips et al. 2016; González-Alfonso et al. 2018). Moreover, testing [C I](1–0) as a sensitive molecular probe in a local and well-studied galaxy such as NGC 6240 has a great legacy value for studies at  $z > 2$ , where the [C I] lines are very valuable tracers of the bulk of the molecular gas accessible with ALMA (Zhang et al. 2016).

The paper is organized as follows. In Section 2 we describe the data. In Section 3.1 we present the CO(1–0), CO(2–1), and [C I] (1–0) outflow maps and the [C I](1–0) line moment maps. In Sections 3.2–3.3 we identify the outflowing components of the molecular line emission and derive the  $\alpha_{CO}$  and  $r_{21}$  values separately for the quiescent ISM and the outflow. The outflow energetics are constrained in Section 3.4. In Section 3.5 we study the variations of  $\alpha_{CO}$  and  $r_{21}$  as a function of  $\sigma_v$  and distance of the different spectral components from the nucleus. Our findings are discussed in Section 4 and summarized in Section 5. Throughout the paper, we adopt a standard  $\Lambda$ CDM cosmological model with  $H_0 = 67.8 km s^{-1} Mpc^{-1}$ ,  $\Omega_\Lambda = 0.692$ ,  $\Omega_M = 0.308$  (Planck Collaboration et al. 2016). At the distance of NGC 6240 (redshift  $z = 0.02448$ , luminosity distance  $D_L = 110.3 Mpc$ ), the physical scale is  $0.509 kpc arcsec^{-1}$ . Uncertainties correspond to  $1\sigma$  statistical errors. The units of  $\alpha_{CO} [M_\odot (K km s^{-1} pc^2)^{-1}]$  are sometimes omitted.

## 2. Observations

The Band 8 observations of the [C I](1–0) ( $\nu_{rest}^{[C I]} = 492.16065$  GHz) emission line in NGC 6240 were carried out in 2016 May with the 12 m diameter antennas of ALMA, and in 2016 August with the 7 m diameter antennas of the Atacama Compact Array

<sup>16</sup> By using the CO(2–1) transition.

<sup>17</sup> CO(1–0) and [C I](1–0) are similar in critical density, but  $E_{10}/k_B = 5.5 K$  for CO and  $23 K$  for [C I]; however, as long as most of the  $H_2$  gas has  $T_k > 15\text{--}20 K$ , as expected, the  $E/k_B$  difference between the two lines makes no real excitation difference in the level population (Papadopoulos et al. 2004).

(ACA) as part of our Cycle 3 programme 2015.1.00717.S (PI: Cicone). The ALMA observations were effectuated in a compact configuration with 40 antennas (minimum and maximum baselines,  $b_{\min} = 15$  m,  $b_{\max} = 640$  m), yielding an angular resolution (AR) of  $0''.24$  and a maximum recoverable scale (MRS) of  $2''.48$ . Only one of the two planned 0.7-hour-long scheduling blocks was executed, and the total on-source time was 0.12 hours. The PWV was 0.65 mm, and the average system temperature was  $T_{\text{sys}} = 612$  K. The ACA observations were performed using nine antennas with  $b_{\min} = 9$  m and  $b_{\max} = 45$  m, resulting in  $\text{AR} = 2''.4$  and  $\text{MRS} = 14''$ . The total ACA observing time was 3.5 hours, with 0.7 hours on source. The average PWV and  $T_{\text{sys}}$  were 0.7 mm and 550 K, respectively. J1751+0939 and Titan were used for flux calibration, J1924-2914 for bandpass calibration, and J1658+0741 and J1651+0129 for phase calibration.

We employed the same spectral setup for the ALMA and the ACA observations. Based on previous CO(1–0) observations of NGC 6240 (Feruglio et al. 2013a, 2013b), and on the knowledge of the concurrence of the [C I](1–0) and CO(1–0) emissions, we expected the [C I](1–0) line to be significantly broad (full width at zero intensity,  $\text{FWZI} > 1000 \text{ km s}^{-1}$ ). Therefore, to recover both the broad [C I](1–0) line and its adjacent continuum, we placed two spectral windows at a distance of 1.8 GHz, overlapping by 75 MHz in their central 1.875 GHz wide full sensitivity part, yielding a total bandwidth of 3.675 GHz ( $2293 \text{ km s}^{-1}$ ) centered at  $\nu_{\text{obs}}^{\text{[C I]}} = 480.40045$  GHz.

After calibrating separately the ALMA and ACA data sets with the respective scripts delivered to the PI, we fit and subtracted the continuum in the  $uv$  plane. This was done through the CASA<sup>18</sup> task `uvcontsub`, by using a zeroth-order polynomial for the fit, and by estimating the continuum emission in the following line-free frequency ranges:  $478.568 < \nu_{\text{obs}} [\text{GHz}] < 478.988$  and  $481.517 < \nu_{\text{obs}} [\text{GHz}] < 482.230$ . The line visibilities were then deconvolved using `clean` with Briggs weighting and robust parameter equal to 0.5. A spectral binning of  $\Delta\nu = 9.77 \text{ MHz}$  ( $6 \text{ km s}^{-1}$ ) was applied, and the cleaning masks were chosen interactively. In order to improve the image reconstruction, following the strategy adopted by Hacar et al. (2018), we used the cleaned ACA data cube corrected for primary beam as a source model to initialize the deconvolution of the ALMA line visibilities (parameter “`modelimage`” in `clean`). The synthesized beams of the resulting ACA and ALMA image data cubes are  $4''.55 \times 2''.98$  ( $\text{PA} = -53^\circ 57'$ ) and  $0''.29 \times 0''.24$  ( $\text{PA} = 113^\circ 18'$ ), respectively. In addition, a lower resolution ALMA [C I](1–0) line data cube was produced by applying a tapering (outer taper of  $1''.4$ ), which resulted in a synthesized beam of  $1''.28 \times 1''.02$  ( $\text{PA} = 77^\circ 49'$ ). Primary beam correction was applied to all data sets. We checked the accuracy of the ALMA and ACA relative flux scales by comparing the flux on the overlapping spatial scales between the two arrays, and found that they are consistent within the Band 8 calibration uncertainty of 15%.

As a last step, in order to maximize the  $uv$  coverage and the sensitivity to any extended structure possibly filtered out by the ALMA data, we combined the (tapered and non) ALMA image data cubes with the ACA one using the task `feather`. For a detailed explanation of `feather`, we refer the reader to the

CASA cookbook.<sup>19</sup> The same steps were used to produce all the interferometric maps shown in this paper: (1) `clean` of ACA visibilities followed by primary beam correction, (2) `clean` of ALMA visibilities by using the ACA images as a source model followed by primary beam correction, and (3) `feather` of the ACA and ALMA images. The resulting ACA+ALMA merged images inherit the synthesized beam and cell size (the latter set equal to  $0''.01$  and  $0''.2$ , respectively, for the higher and lower resolution data) of the corresponding input ALMA images. At the phase tracking center (central beam), the  $1\sigma$  sensitivities to line detection, calculated using the line-free spectral channels, are  $1.4 \text{ mJy beam}^{-1}$  and  $5 \text{ mJy beam}^{-1}$  per  $d\nu = 50 \text{ km s}^{-1}$  spectral channel, respectively, for the higher and lower resolution [C I](1–0) line data cubes. The sensitivity decreases slightly with distance from the phase center. At a radius of  $5''$ , the [C I](1–0) line sensitivities per  $d\nu = 50 \text{ km s}^{-1}$  spectral channel are  $3.3 \text{ mJy beam}^{-1}$  and  $5.5 \text{ mJy beam}^{-1}$ .

In this paper we make use of the IRAM PdBI CO(1–0) data previously presented by Feruglio et al. (2013a, 2013b). The CO(1–0) line image data cube used in this analysis has a synthesized beam of  $1''.42 \times 1''.00$  ( $\text{PA} = 56^\circ 89'$ ) and a cell size of  $0''.2$ . The CO(1–0)  $1\sigma$  line sensitivity per  $d\nu = 50 \text{ km s}^{-1}$  spectral channel is  $0.6 \text{ mJy beam}^{-1}$  at the phase center, and  $0.65 \text{ mJy beam}^{-1}$  at a  $5''$  radius.

Our analysis also includes ALMA Band 6 (programme 2015.1.00370.S, PI: Treister) snapshot (1 minute on source) observations of NGC 6240 targeting the CO(2–1) transition, which were performed in 2016 January (PWV = 1.2 mm) using the compact configuration ( $\text{AR} = 1''.2$ ,  $\text{MRS} = 10''$ ). These observations were executed in support of the long baseline campaign carried out by E. Treister et al. (2018, in preparation). We calibrated the data using the script for PI, estimated the continuum from the line-free spectral ranges ( $224.106 < \nu_{\text{obs}} [\text{GHz}] < 224.279$  and  $225.780 < \nu_{\text{obs}} [\text{GHz}] < 225.971$ ), and subtracted it in the  $uv$  plane. We deconvolved the line visibilities using `clean` with Briggs weighting (robust = 0.5) and applied a correction for primary beam. The final CO(2–1) cleaned data cube has a synthesized beam of  $1''.54 \times 0''.92$  ( $\text{PA} = 60^\circ 59'$ ) and a cell size of  $0''.2$ . The  $1\sigma$  CO(2–1) line sensitivity per  $d\nu = 50 \text{ km s}^{-1}$  channel is  $0.80 \text{ mJy beam}^{-1}$  at the phase center and  $1 \text{ mJy beam}^{-1}$  at a  $5''$  radius.

In the analysis that follows, the comparison between the CO(1–0), CO(2–1), and [C I](1–0) line tracers in the molecular outflow of NGC 6240 will be done by using the lower resolution ALMA+ACA [C I](1–0) data cube, which matches in AR ( $\sim 1''.2$ ) the IRAM PdBI CO(1–0) and ALMA CO(2–1) data. Unless specified, quoted errors include the systematic uncertainties on the measured fluxes due to flux calibration, which are 10% for the IRAM PdBI CO(1–0) and ALMA CO(2–1) data, and 15% for the ALMA [C I](1–0) line observations. We report the presence of some negative artifacts, especially in the cleaned CO(1–0) and CO(2–1) data cubes. These are due to the interferometric nature of the observations, which does not allow to properly recover all the faint extended emission in a source with a very bright central peak emission such as NGC 6240. However, the negative features lie mostly outside the region probed by our analysis, and they are not expected to significantly affect our flux recovery, since the total

<sup>18</sup> Common Astronomy Software Applications (McMullin et al. 2007).

<sup>19</sup> Available at <https://casa.nrao.edu>.



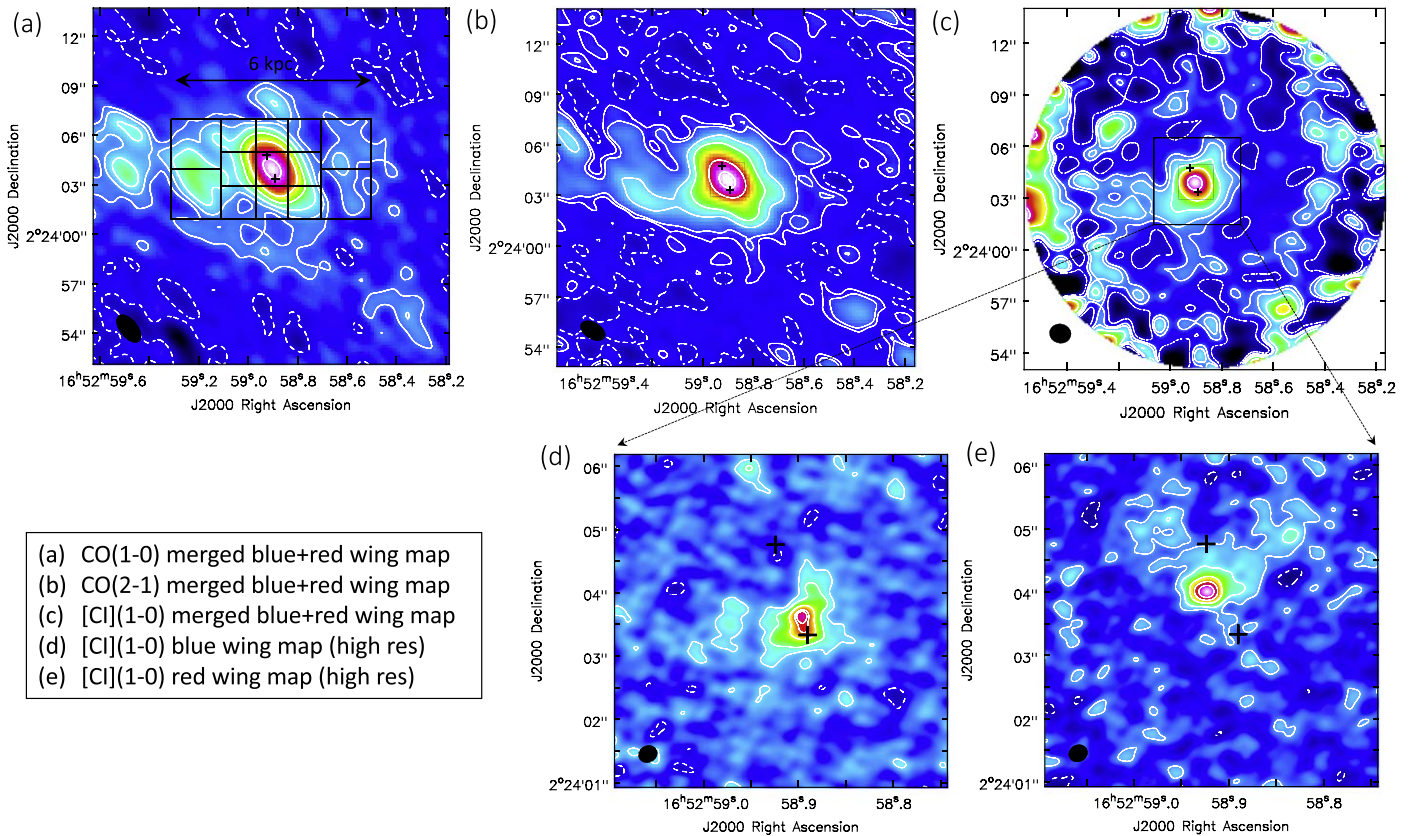


**Figure 1.** Extended NGC 6240 outflow observed using different molecular gas tracers. The outflow emission, integrated within  $v \in (-650, -200)$  km s $^{-1}$  (blue wing) and  $v \in (250, 800)$  km s $^{-1}$  (red wing) and combined together, is shown in the maps (a)–(c), respectively, for the CO(1–0), CO(2–1), and [C I](1–0) transitions. The three maps have matched spatial resolution ( $\sim 1''.2$ , details in Section 2). Contours correspond to  $(-3\sigma, 3\sigma, 6\sigma, 12\sigma, 24\sigma, 48\sigma, 200\sigma, 400\sigma)$  with  $1\sigma = 0.14$  mJy beam $^{-1}$  in panel (a);  $(-3\sigma, 3\sigma, 6\sigma, 12\sigma, 24\sigma, 48\sigma, 150\sigma)$  with  $1\sigma = 0.23$  mJy beam $^{-1}$  in panel (b);  $(-3\sigma, 3\sigma, 6\sigma, 12\sigma, 24\sigma, 48\sigma)$  with  $1\sigma = 1.23$  mJy beam $^{-1}$  in panel (c). Panels (d) and (e) show the maps of the [C I](1–0) blue and red wings at the original spatial resolution of the ALMA Band 8 data ( $0''.24$ , details in Section 2). Contours correspond to  $(-3\sigma, 3\sigma, 6\sigma, 12\sigma, 18\sigma, 20\sigma)$  with  $1\sigma = 1.1$  mJy beam $^{-1}$  in panel (d) and  $1\sigma = 1$  mJy beam $^{-1}$  in panel (e). The black crosses indicate the VLBI positions of the AGNs from Hagiwara et al. (2011). The synthesized beams are shown at the bottom-left of each map. The grid encompassing the central  $12'' \times 6''$  region and employed in the spectral analyses presented in Sections 3.2 and 3.3 is drawn in panel (a).

CO(1–0) and CO(2–1) line fluxes are consistent with previous single-dish measurements (Costagliola et al. 2011; Papadopoulos et al. 2012b). Our total [C I](1–0) line flux is higher than that recovered by Papadopoulos and Greve (2004) by using the James Clerk Maxwell telescope (JCMT,  $\text{FWHM}_{\text{beam}} = 10''$ ), but lower by  $34 \pm 15\%$  than the flux measured by the *Herschel Space Observatory* (Papadopoulos et al. 2014). This indicates that some faint extended emission has been resolved out and/or that there is additional [C I](1–0) line emission outside the field of view of our observations.

### 3. Data Analysis and Results

#### 3.1. Morphology of the Extended Molecular Outflow and Its Launch Region

With the aim of investigating the extent and morphology of the outflow, we produced interferometric maps of the CO(1–0), CO(2–1), and [C I](1–0) high-velocity emissions. The maps, shown in Figures 1(a)–(c), were generated by merging together and imaging the  $uv$  visibilities corresponding to the blue- and redshifted wings of the molecular lines, integrated respectively within  $v \in (-650, -200)$  km s $^{-1}$  and  $v \in (250, 800)$  km s $^{-1}$ . These are the velocity ranges that, following from the identification of the outflow components performed in Section 3.3 (and further discussed in Section 4.1 and

Appendix B), are completely dominated by the emission from outflowing gas. The data displayed in panels (a)–(c) have a matched spatial resolution equal to  $\sim 1''.2$  (details in Section 2). Panels (d), (e) of Figure 1 show the maps of the blue and red [C I](1–0) line wings at the native spatial resolution of the ALMA Band 8 observations ( $0''.24$ , Section 2).

The extended ( $>5$  kpc) components of the outflow are best seen in Figures 1(a)–(c), whereas panels (d), (e) provide a zoomed view of the molecular wind in the inner 1–2 kpc. The bulk of the outflow extends eastward of the two AGNs, as already pointed out in the previous analysis of the CO(1–0) data done by Feruglio et al. (2013a). In addition, we identify for the first time a western extension of the molecular outflow, roughly aligned along the same east–west axis as the eastern component. At the sensitivity allowed by our data, we detect at a  $\text{S/N} > 5$  CO emission features associated with the outflow up to a maximum distance of  $13''.3$  (6.8 kpc) and  $7''.2$  (3.7 kpc) from the nucleus, respectively, in the east and west directions (Figure 1(a)–(c)). The [C I](1–0) map in Figure 1(c) shows extended structures similar to CO, although the limited field of view of the Band 8 observations does not allow us to probe emission beyond a radius of  $\sim 7''.5$ .

Feruglio et al. (2013a) hinted at the possibility that the redshifted CO detected in NGC 6240 could be involved in the feedback process, but did not explicitly ascribe it to the outflow because of the smaller spatial extent of the red wing with

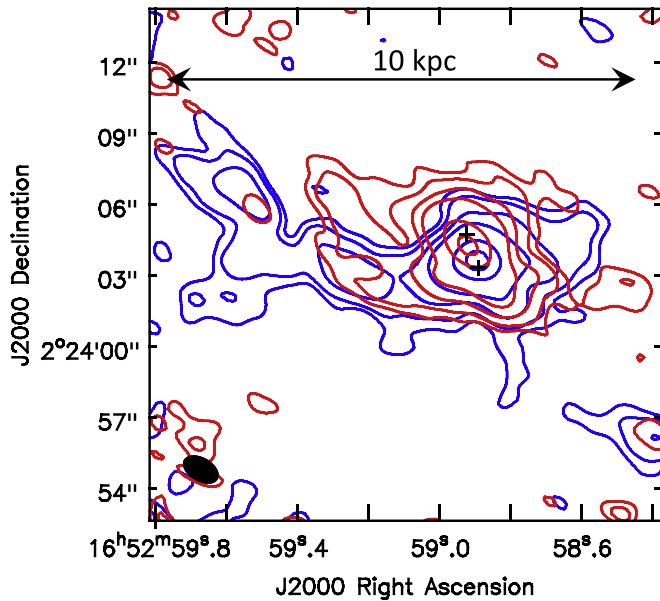


**Figure 2.** Comparison between the CO(2–1) blue and red wing emissions in NGC 6240. For visualization purposes, only positive contours starting from  $5\sigma$  are shown, with  $1\sigma = 0.33 \text{ mJy beam}^{-1}$  for the blue wing (blue contours) and  $1\sigma = 0.3 \text{ mJy beam}^{-1}$  for the red wing (red contours). The corresponding interferometric maps including negative contours are displayed in Appendix A (Figure 7).

respect to the blue wing. In Figure 2 we directly compare the blue and red line wings using the ALMA CO(2–1) data. Based on their close spatial correspondence, whereby the red wing overlaps with the blue one across more than 7 kpc along the east–west direction, we conclude that both the redshifted and blueshifted velocity components trace the same massive molecular outflow. It follows that the eastern and western sides of the outflow are detected in both their approaching and receding components. At east, the blueshifted emission is brighter than the redshifted one and dominant beyond a 3.5 kpc radius.

The ALMA [C I](1–0) data can be used to identify with high precision the location of the inner portion of the molecular outflow. Figures 1(d), (e) clearly show that the red wing peaks in the midpoint between the two AGNs, and that the blue wing has a maximum of intensity closer to the southern AGN, as already noted by Feruglio et al. (2013a). However, these data reveal for the first time that neither the blue nor the redshifted high-velocity [C I](1–0) emissions peak exactly at the AGN positions. The blue wing has a maximum of intensity at R.A.(J2000) =  $16:52:58.8946 \pm 0.0011\text{s}$ , decl.(J2000) =  $+02:24:03.52 \pm 0''02$ , offset by  $0''18 \pm 0''02$  to the north-east with respect to the southern AGN. The red wing instead peaks at R.A.(J2000) =  $16:52:58.9224 \pm 0.0007\text{s}$ , decl.(J2000) =  $+02:24:04.0158 \pm 0''007$  (i.e., at an approximately equal distance of  $0''8$  from the two AGNs). The [C I](1–0) red and blue wing peaks are separated by  $0''65 \pm 0''02$ . This separation is consistent with the distance between the CO(2–1) peaks reported by Tacconi et al. (1999), although in that work they were interpreted as the signature of a rotating molecular gas disk.

The presence of such nuclear rotating  $\text{H}_2$  structure has been largely debated in the literature, especially due to the very high CO velocity dispersion in this region ( $\sigma > 300 \text{ km s}^{-1}$ ), and to the mismatch between the dynamics of  $\text{H}_2$  gas and stars (Geressen et al. 2004; Engel et al. 2010). Following

Tacconi et al. (1999) and Bryant and Scoville (1999), if a rotating disk is present, its signature should appear at *lower* projected velocities than those imaged in Figures 1(d), (e). In Figure 3 we show the high resolution intensity-weighted moment maps of the [C I](1–0) line emission within  $-200 < v[\text{km s}^{-1}] < 250$ . The velocity field does not exhibit the characteristic butterfly pattern of a rotating disk, but it presents a highly asymmetric gradient whereby blueshifted velocities dominate the southern emission, whereas near-systemic and redshifted velocities characterize the northern emission. These features in the velocity field are correlated in both velocity and position with the high-velocity wings (Figures 1(d), (e)). Furthermore, the right panel of Figure 3 shows that the velocity dispersion is uniform ( $50 \lesssim \sigma_v[\text{km s}^{-1}] \lesssim 80$ ) throughout the entire source and enhanced ( $\sigma_v \geq 100 \text{ km s}^{-1}$ ) in a central hourglass-shaped structure extending east–west, which is the same direction of expansion of the larger-scale outflow. This structure has a high- $\sigma_v$  peak with  $\sigma_v \geq 150 \text{ km s}^{-1}$  to the east and another possible peak to the west with  $\sigma_v \geq 130 \text{ km s}^{-1}$ . Such high- $\sigma_v$  points coincide with the blue and redshifted velocity peaks detected in the moment 1 map. Therefore, based on Figure 3, we conclude that the molecular gas emission between the two AGNs is dominated by a nuclear outflow expanding east–west and connected to the larger-scale outflow shown in Figure 1. The regions of enhanced turbulence may represent the places where the outflow opening angle widens up, hence increasing the line of sight velocity dispersion and velocity of the molecular gas.

### 3.2. The $\alpha_{\text{CO}}$ Values Estimated from the Integrated Spectra: A Reference for Unresolved Studies

Figure 4 shows the CO(1–0), CO(2–1), and [C I](1–0) spectra extracted from the  $12'' \times 6''$ -size rectangular aperture reported in Figure 1(a), encompassing both the nucleus and the extended molecular outflow of NGC 6240. The analysis of these integrated spectra, described later, is aimed at deriving a source-averaged  $\alpha_{\text{CO}}$  for the quiescent and outflowing molecular ISM in NGC 6240. Such analysis is included here because it can be useful as a reference for unresolved observations (e.g., high redshift analogues of this merger). We stress, however, that the quality of our data, the proximity of the source, and its large spatial extent allow us to perform a much more detailed, spatially resolved analysis. The latter will be presented in Section 3.3 and delivers the most reliable  $\alpha_{\text{CO}}$  values for the outflow and the quiescent gas.

The spectra in Figure 4 were fitted simultaneously using two Gaussians to account for the narrow core and broad wings of the emission lines, by constraining the central velocity ( $v$ ) and velocity dispersion ( $\sigma_v$ ) of each Gaussian to be equal in the three transitions. Table 1 reports the best fit results and the corresponding line luminosities calculated from the integrated fluxes following Solomon et al. (1997). The [C I](1–0) line luminosities listed in Table 1 are employed to measure the molecular gas mass ( $M_{\text{mol}}$ , including the contribution from helium) associated with the narrow and broad line components. The expression for local thermodynamic equilibrium (LTE; i.e., uniform  $T_{\text{ex}}$ ) and optically thin emission ( $\tau_{[\text{C I}](1-0)} \ll 1$ ), assuming a negligible background (CMB temperature,  $T_{\text{CMB}} \ll T_{\text{ex}}$ ) and the Rayleigh–Jeans



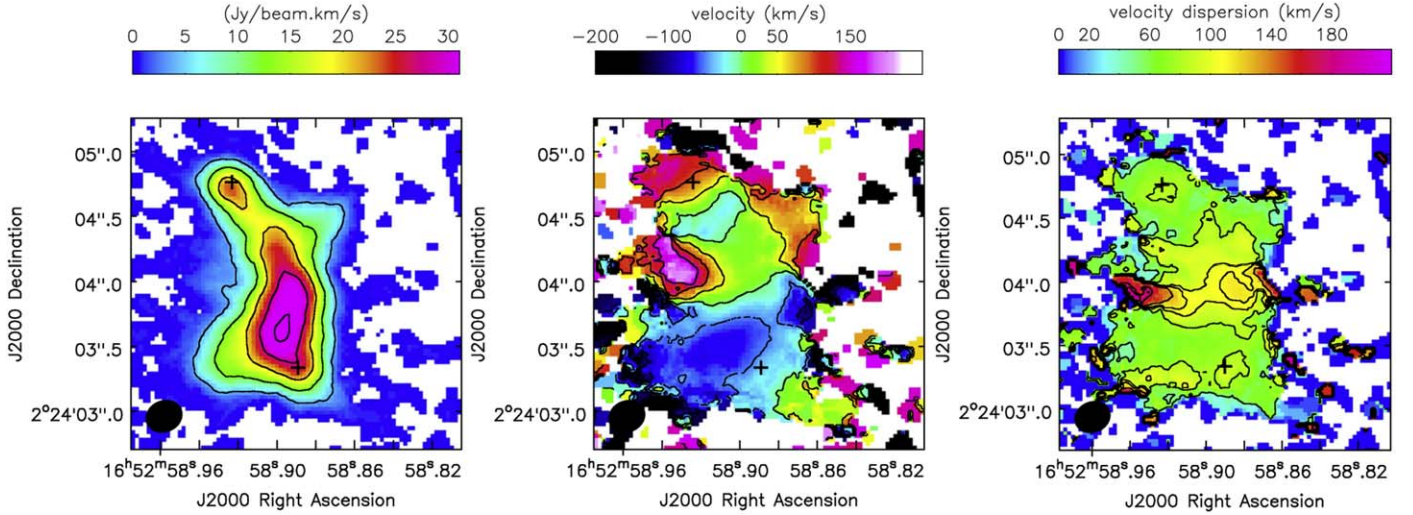


**Figure 3.** Intensity-weighted moment maps of the [C I](1–0) line emission in the merger nucleus. The maps were computed from the higher resolution ALMA+ACA merged data cube (see Section 2) by using the task `immoments` and by selecting the spectral range  $v \in (-200, 250)$  km s<sup>-1</sup>. Contours correspond to  $[-100, -50, 0, 50, 100, 150]$  km s<sup>-1</sup> (moment 1, central panel) and  $[50, 80, 100, 110, 130, 170, 180]$  km s<sup>-1</sup> (moment 2, right panel).

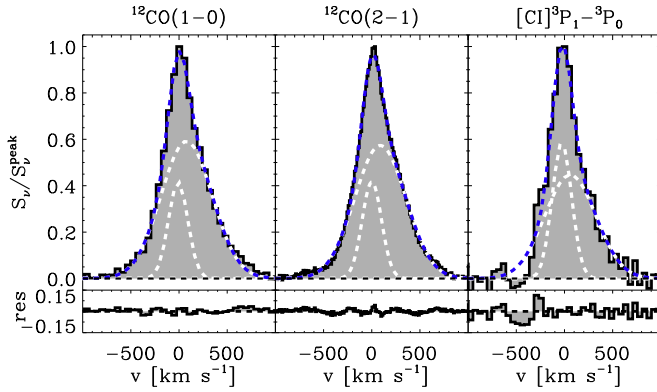


**Figure 4.** Total CO(1–0), CO(2–1), and [C I](1–0) spectra extracted from a  $12'' \times 6''$ -size rectangular region centered at R.A. = 16:52:58.900, decl. = 02:24:03.950, and displayed in Figure 1(a). The rms values per spectral channel are 3.2 mJy ( $\delta v = 53$  km s<sup>-1</sup>), 17 mJy ( $\delta v = 13$  km s<sup>-1</sup>), and 78 mJy ( $\delta v = 49$  km s<sup>-1</sup>), respectively, for CO(1–0), CO(2–1), and [C I](1–0). The spectra were simultaneously fitted using two Gaussian functions (white dashed curves) tied to have the same velocity and width in all three transitions. The best fit results are reported in Table 1. The source-averaged  $r_{21}$  and  $\alpha_{CO}$  calculated from this fit are listed in Table 2.

approximation ( $h\nu_{C\,I(1-0)} \ll kT_{ex}$ ), is

$$M_{mol}[M_{\odot}] = (4.31 \cdot 10^{-5}) \cdot X_{C\,I}^{-1} \cdot (1 + 3e^{-23.6/T_{ex}[K]} + 5e^{-62.5/T_{ex}[K]}) \cdot e^{23.6/T_{ex}[K]} \cdot L'_{[C\,I](1-0)} [K \, km \, s^{-1} \, pc^2], \quad (1)$$

where  $X_{C\,I}$  is the [C I]/H<sub>2</sub> abundance ratio and  $T_{ex}$  is the excitation temperature of the gas (see detailed explanations by Papadopoulos et al. 2004 and Mangum & Shirley 2015). We adopt  $T_{ex} = 30$  K and  $X_{C\,I} = (3.0 \pm 1.5) \times 10^{-5}$ , which are appropriate for (U)LIRGs (Weiß et al. 2003, 2005; Papadopoulos et al. 2004; Walter et al. 2011; Jiao et al. 2017). These assumptions will be further discussed in Section 4.1.2.

By defining a [C I](1–0)-to-H<sub>2</sub> conversion factor ( $\alpha_{[C\,I]}$ ) in analogy with the commonly employed  $\alpha_{CO}$  factor

**Table 1**  
Results of the Simultaneous Fit to the Total Spectra<sup>a</sup>

	CO(1–0)	CO(2–1)	[C I](1–0)
Narrow component			
$v^b$ [km s <sup>-1</sup> ]	$-9.1 \pm 1.0$	$-9.1 \pm 1.0$	$-9.1 \pm 1.0$
$\sigma_v$ [km s <sup>-1</sup> ]	$101.0 \pm 1.0$	$101.0 \pm 1.0$	$101.0 \pm 1.0$
$S_{peak}$ [mJy]	$211 \pm 4$	$1058 \pm 12$	$1360 \pm 70$
$\int S_v dv$ [Jy km s <sup>-1</sup> ]	$53.4 \pm 1.0$	$268 \pm 4$	$344 \pm 18$
$L'$ [ $10^9$ K km s <sup>-1</sup> pc <sup>2</sup> ]	$1.55 \pm 0.03$	$1.94 \pm 0.03$	$0.55 \pm 0.03$
Broad component			
$v^b$ [km s <sup>-1</sup> ]	$78.0 \pm 1.2$	$78.0 \pm 1.2$	$78.0 \pm 1.2$
$\sigma_v$ [km s <sup>-1</sup> ]	$264.4 \pm 1.0$	$264.4 \pm 1.0$	$264.4 \pm 1.0$
$S_{peak}$ [mJy]	$301 \pm 3$	$1458 \pm 12$	$1040 \pm 40$
$\int S_v dv$ [Jy km s <sup>-1</sup> ]	$199 \pm 2$	$966 \pm 9$	$690 \pm 30$
$L'$ [ $10^9$ K km s <sup>-1</sup> pc <sup>2</sup> ]	$5.78 \pm 0.06$	$7.01 \pm 0.06$	$1.09 \pm 0.05$
Total line			
$\int S_v dv$ [Jy km s <sup>-1</sup> ]	$253 \pm 2$	$1234 \pm 10$	$1030 \pm 30$
$L'$ [ $10^9$ K km s <sup>-1</sup> pc <sup>2</sup> ]	$7.33 \pm 0.07$	$8.96 \pm 0.07$	$1.64 \pm 0.05$

#### Notes.

<sup>a</sup> The errors quoted in this table are purely statistical and do not include the absolute flux calibration uncertainty.

<sup>b</sup> We employ the optical Doppler definition. The fit allows for a global velocity shift of CO(2–1) and [C I](1–0) with respect to CO(1–0) to take into account the different spectral binning. The best fit returns:  $v_{CO(2-1)} - v_{CO(1-0)} = 10.2 \pm 0.9$  km s<sup>-1</sup> and  $v_{[C\,I](1-0)} - v_{CO(1-0)} = -18 \pm 4$  km s<sup>-1</sup>.

(Bolatto et al. 2013), Equation (1) resolves into

$$M_{mol}[M_{\odot}] \equiv \alpha_{[C\,I]} L'_{[C\,I]} [K \, km \, s^{-1} \, pc^2] \quad \text{with } \alpha_{[C\,I]} = 9.43 [M_{\odot} (K \, km \, s^{-1} \, pc^2)^{-1}]. \quad (2)$$

Using the values in Table 1 and Equation (2), we obtain a total molecular gas mass of  $M_{mol} = (1.5 \pm 0.8) \cdot 10^{10} M_{\odot}$ , of which  $(5 \pm 3) \cdot 10^9 M_{\odot}$  is in the narrow component, and  $(10 \pm 5) \cdot 10^9 M_{\odot}$  in the broad wings. We then use these  $M_{mol}$

**Table 2**  
 $\alpha_{\text{CO}}$  and  $r_{21}$  Values<sup>a</sup>

	$\alpha_{\text{CO}}$ [ $M_{\odot} (\text{K km s}^{-1} \text{ pc}^2)^{-1}$ ]	$r_{21}$
Total <sup>b</sup>	$2.1 \pm 1.1$	$1.22 \pm 0.14$
Total <sup>b</sup> narrow comp	$3.3 \pm 1.8$	$1.25 \pm 0.18$
Total <sup>b</sup> broad comp	$1.8 \pm 0.9$	$1.21 \pm 0.17$
Mean <sup>c</sup> global	$2.5 \pm 1.4$	$1.17 \pm 0.19$
Mean <sup>c</sup> systemic comp	$3.2 \pm 1.8$	$1.0 \pm 0.2$
Mean <sup>c</sup> outflow comp	$2.1 \pm 1.2$	$1.4 \pm 0.3$

**Notes.**

<sup>a</sup> Quoted errors are dominated by systematic uncertainties (e.g., absolute flux calibration errors, error on  $X_{\text{C I}}$ ).

<sup>b</sup> Calculated from the simultaneous fit to the total CO(1–0), CO(2–1), and [C I](1–0) spectra shown in Figure 4, whose results are reported in Table 1 (details in Section 3.2).

<sup>c</sup> Mean values calculated from the simultaneous fit to the CO(1–0), CO(2–1), and [C I](1–0) spectra extracted from the grid of 13 boxes shown in Figure 1(a), as explained in Section 3.3. The corresponding spectral fits are shown in Appendix B (Figures 8–10).

values to estimate  $\alpha_{\text{CO}}$ :

$$\alpha_{\text{CO}} = M_{\text{mol}} [M_{\odot}] (L'_{\text{CO}(1-0)} [\text{K km s}^{-1} \text{ pc}^2])^{-1}. \quad (3)$$

The results are reported in the first three rows of Table 2 for the total, narrow, and broad emissions in NGC 6240. The so-derived  $\alpha_{\text{CO}}$  factors differ between the narrow and broad line components, being a factor of  $1.8 \pm 0.5$  lower in the latter.<sup>20</sup> In the narrow component, the  $\alpha_{\text{CO}}$  is significantly higher than the typical (U)LIRG value. As mentioned in Section 1, higher  $\alpha_{\text{CO}}$  values become possible in (U)LIRGs if a significant fraction of the mass is “hidden” in dense and bound  $\text{H}_2$  clouds. This is probably the case of NGC 6240, in which a large study using CO SLEDs from  $J = 1-0$  up to  $J = 13-12$  from the *Herschel Space Observatory*, as well as multi- $J$  HCN, CS, and  $\text{HCO}^+$  line data from ground-based observatories, finds  $\alpha_{\text{CO}} \sim 2-4 M_{\odot} (\text{K km s}^{-1} \text{ pc}^2)^{-1}$  (Papadopoulos et al. 2014), consistent with our estimates.

Table 2 lists also the CO(2–1)/CO(1–0) luminosity ratios, defined as

$$r_{21} \equiv L'_{\text{CO}(2-1)} / L'_{\text{CO}(1-0)}. \quad (4)$$

We find  $r_{21}$  as consistently  $\sim 1.2$ —hence higher than unity (at the  $1.5\sigma$  level)—for both the narrow and broad Gaussian components. Since our total CO(1–0) and CO(2–1) fluxes are consistent with previous measurements (Costagliola et al. 2011; Papadopoulos et al. 2012b; Saito et al. 2018), we exclude that spatial filtering due to an incomplete  $uv$  coverage is significantly affecting the  $r_{21}$  values. As pointed out by Papadopoulos et al. (2012b), galaxy-averaged  $r_{21} > 1$  values are not uncommon in (U)LIRGs and are indicative of extreme gas conditions. In this analysis of the integrated spectra, we derived  $r_{21} > 1$  in both the broad and narrow components. However, as we will show in Sections 3.3 and 3.5, the spatially resolved analysis will reveal that  $r_{21} \gtrsim 1$  values are typical of

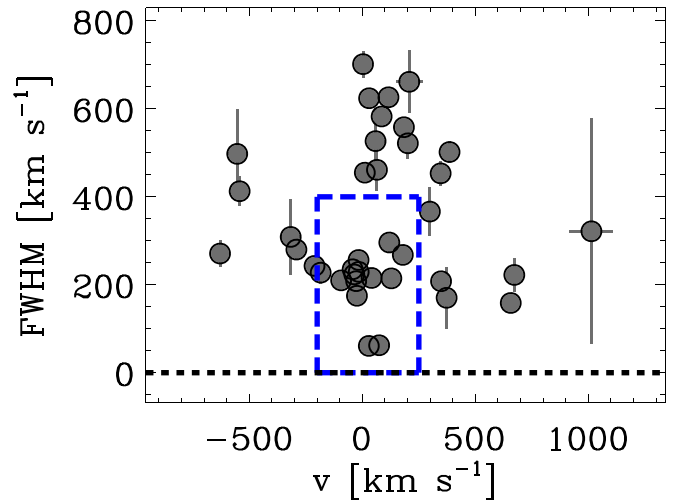


**Figure 5.** FWHM as a function of central velocity of all Gaussian components employed in the simultaneous fitting of the CO(1–0), CO(2–1), and [C I](1–0) box spectra. The blue dashed rectangle constrains the region of the parameter space that we ascribe to the “systemic” components.

the outflowing gas and in general of higher- $\sigma_v$  components, while the “quiescent” ISM has  $r_{21} \sim 1$ .

### 3.3. Spatially Resolved Analysis: The Average $\alpha_{\text{CO}}$ of the Quiescent and Outflowing Gas

The previous analysis (Section 3.2) was based on the spectral fit shown in Figure 4, where we decomposed the total molecular line emission into a narrow and a broad Gaussian. In first approximation, these two spectral components can be respectively identified with the quiescent and outflowing molecular gas reservoirs of NGC 6240. However, the superb S/N and spatial resolution of our data allow us to take this analysis one step further and refine the definition of quiescent and outflowing components. This is done by including the spatially resolved information provided by the interferometric data, as described later.

We divide the central  $12'' \times 6''$  region employed in the previous analysis into a grid of 13 squared boxes and use them as apertures to extract the corresponding CO(1–0), CO(2–1), and [C I](1–0) spectra. As shown in Figure 1(a), the central nine boxes have a size of  $2'' \times 2''$ , while the external four boxes have a size of  $3'' \times 3''$ . The box spectra are presented in Appendix B (Figures 8–10).

For each box, the CO(1–0), CO(2–1), and [C I](1–0) spectra are fitted simultaneously with a combination of Gaussian functions tied to have the same line centers and widths for all three transitions. In the fitting procedure, we minimize the number of spectral components required to reproduce the line profiles, up to a maximum of four Gaussians per box. The Gaussian functions employed by the simultaneous fit span a wide range in FWHM and velocity, shown in Figure 5. The next step is to classify each of these components as “systemic” or “outflow.” In many local (U) LIRGs, molecular outflows can be traced through components whose kinematical and spatial features deviate from a rotating molecular structure (Cicone et al. 2014; García-Burillo et al. 2014). However, in this source we do not detect any clear velocity gradient that may indicate the presence of a rotating molecular gas disk (Figure 3). Therefore, we adopt a different method and identify as “quiescent” the gas probed by the spectral narrow line components that are detected throughout the entire source extent (Figures 8–10). Our simultaneous fit to the CO(1–0), CO(2–1), and

<sup>20</sup> In estimating the error on this ratio, we have ignored the systematic uncertainty on  $X_{\text{C I}}$ , assuming it affects both  $\alpha_{\text{CO}}$  measurements in the same way.

[C I](1–0) spectra returns for these narrow components typical FWHM and central velocities in the ranges:  $\text{FWHM} < 400 \text{ km s}^{-1}$  and  $-200 < v [\text{km s}^{-1}] < 250$ , consistent with what found by Feruglio et al. (2013b).<sup>21</sup> Based on these results, we assume that all components with  $-200 < v [\text{km s}^{-1}] < 250$  and  $\text{FWHM} < 400 \text{ km s}^{-1}$  trace quiescent gas that is not involved in the outflow. These constraints correspond to the region of the FWHM- $v$  parameter space delimited by the blue dashed lines in Figure 5. All components outside this rectangular area are classified as “outflow.” These assumptions are discussed in detail and validated in Appendix B, whereas more general considerations about our outflow identification method are reported in Section 4.1.1.

Using the results of the simultaneous fit, we measure, for each box and for each of the CO(1–0), CO(2–1), and [C I](1–0) transitions, the velocity-integrated fluxes apportioned in the “systemic” and “outflow” components. These are computed by summing the fluxes from the respectively classified Gaussian functions fitted to the molecular line profiles. For example, in the case of the central box (labeled as “C1” in Figures 8–10), the simultaneous fit employs three Gaussians: a narrow one classified as “systemic,” and two additional ones classified as “outflow.” The flux of the first Gaussian corresponds to the flux of the “systemic” component for this box, whereas the total “outflow” component flux is given by the sum of the fluxes of the other two Gaussians (the errors are added in quadrature).

The velocity-integrated fluxes (total, systemic, outflow) are then converted into line luminosities and, from these, the corresponding  $\alpha_{\text{CO}}$  and  $r_{21}$  can be derived by following the same steps as in Section 3.2 (Equations (2)–(4)). Table 2 (bottom three rows) lists the resulting mean values of  $\alpha_{\text{CO}}$  and  $r_{21}$  obtained from the analysis of all 13 boxes. In computing the mean, we only include the components detected at a  $S/N \geq 3$  in each of the transitions used to calculate  $\alpha_{\text{CO}}$  or  $r_{21}$ —that is, CO(1–0) and [C I](1–0) for the former, and CO(1–0) and CO(2–1) for the latter. The new  $\alpha_{\text{CO}}$  values derived for the systemic and outflowing components, respectively equal to  $3.2 \pm 1.8$  and  $2.1 \pm 1.2$ , are perfectly consistent with the previous analysis based on the integrated spectra. Instead, this new analysis delivers different  $\langle r_{21} \rangle$  values for the systemic ( $1.0 \pm 0.2$ ) and outflowing component ( $1.4 \pm 0.3$ ), although still consistent if considering the associated uncertainties (dominated by the flux calibration errors).

By using the CO(1–0) line data and summing the contribution from all boxes, including both the systemic and the outflowing components, we derive a total molecular gas mass of  $M_{\text{mol}}^{\text{tot}} = (2.1 \pm 0.5) \times 10^{10} M_{\odot}$ . To compute the  $M_{\text{mol}}$  within each box we adopt, when available, the “global”  $\alpha_{\text{CO}}$  factor estimated for that same box; otherwise, we use the mean value of  $\alpha_{\text{CO}} = 2.5 \pm 1.4$ .<sup>22</sup> Compared with previous works recovering the same amount of CO flux, our new  $M_{\text{mol}}^{\text{tot}}$  estimate is higher than in Tacconi et al. (1999) and Feruglio et al. (2013a), but consistent with Papadopoulos et al. (2014).

<sup>21</sup> Feruglio et al. (2013b) analyzed the CO(1–0) spectra extracted from different positions within NGC 6240 and found maximum velocity shift and FWHM of the narrow Gaussians of  $|v_{\text{sys}}^{\text{max}}| = 82 \pm 4 \text{ km s}^{-1}$  and  $\text{FWHM}_{\text{sys}} = 380 \pm 150 \text{ km s}^{-1}$ .

<sup>22</sup> This was the case for the three boxes (labeled as “E1,” “W1,” and “W2” in Figures 8–10) without a  $S/N \geq 3$  detection of [C I](1–0).

### 3.4. Molecular Outflow Properties

In this section we use the results of the spatially resolved spectral analysis presented in Section 3.3 to constrain the mass ( $M_{\text{out}}$ ), mass-loss rate ( $\dot{M}_{\text{out}}$ ), kinetic power ( $1/2 \dot{M}_{\text{out}} v^2$ ), and momentum rate ( $\dot{M}_{\text{out}} v$ ) of the molecular outflow. We first select the boxes in which an outflow component is detected in the CO(1–0) spectrum with  $S/N \geq 3$ . As described in Section 3.3, the outflow component is defined as the sum of all Gaussian functions employed by the simultaneous fit that lie outside the rectangular region of the FWHM- $v$  parameter space shown in Figure 5. With this  $S/N \geq 3$  constraint, 12 boxes (that is, all except W1) are selected to have an outflow component in CO(1–0), and for each box,<sup>23</sup> we measure the following:

- (i) The average outflow velocity ( $v_{\text{out},i}$ ), equal to the mean of the (moduli of the) central velocities of the individual Gaussians classified as “outflow”
- (ii) The molecular gas mass in outflow ( $M_{\text{out},i}$ ), calculated by multiplying the  $L'_{\text{CO}(1-0)}$  of each outflow component by an appropriate  $\alpha_{\text{CO}}$ . In ten boxes, the outflow component is detected with  $S/N \geq 3$  also in the [C I](1–0) transition; hence for these boxes we can use their corresponding  $\alpha_{\text{CO}}$  factor (see Section 3.3). For the remaining two boxes (E1 and W2), we adopt the galaxy-averaged outflow  $\alpha_{\text{CO}}$  of  $2.1 \pm 1.2$  (Table 2).
- (iii) The dynamical timescale of the outflow, defined as  $\tau_{\text{dyn},i} = R_i/v_{\text{out},i}$ , where  $R_i$  is the distance of the center of the box from R.A. = 16:52:58.900, decl. = 02:24:03.950. This definition cannot be applied to the central box (C1) because the so-estimated  $R$  would be zero, hence boosting the mass-loss rate to infinite. Therefore, for box C1, we conservatively assume that most of the outflow emission comes from a radius of  $1''$ ; hence we set  $R = 0.5 \text{ kpc}$ . For all boxes, we assume the uncertainty on  $R_i$  to be  $0''.6$  ( $0.3 \text{ kpc}$ ), which is half a beam size.
- (iv) The mass-loss rate  $\dot{M}_{\text{out},i}$ , equal to  $M_{\text{out},i}/\tau_{\text{dyn},i}$

All uncertainties are derived by error propagation.

The resulting total outflow mass and mass-loss rate, obtained by adding the contribution from all boxes, are respectively  $M_{\text{out}} = (1.2 \pm 0.3) \times 10^{10} M_{\odot}$  and  $dM_{\text{out}}/dt = 2500 \pm 1200 M_{\odot} \text{ yr}^{-1}$ . As discussed in Appendix B, the largest contribution to both  $\dot{M}_{\text{out}}$  and its uncertainty is given by the central box. Indeed, box C1 has at the same time the highest estimated  $M_{\text{out}}$  and the smallest—and most uncertain— $R$ , because the outflow is launched from within this region, likely close to the midpoint between the two AGNs, as suggested by Figures 1(d), (e).

Similar to the mass-loss rate, we calculate the total kinetic power and momentum rate of the outflow by summing the contribution from all boxes with a CO(1–0) outflow component, and we obtain, respectively,  $1/2 \dot{M}_{\text{out}} v_{\text{out}}^2 \equiv \sum_i 1/2 \dot{M}_{\text{out},i} v_{\text{out},i}^2 = (0.033 \pm 0.019) L_{\text{AGN}}$  and  $v \dot{M}_{\text{out}} \equiv \sum_i v_i \dot{M}_{\text{out},i} = (80 \pm 50) L_{\text{AGN}}/c$ . If all the gas carried by the outflow escaped the system and the mass-loss continued at the current rate, the depletion timescale of the molecular gas reservoir in NGC 6240 would be  $\tau_{\text{dep}} = 8 \pm 4 \text{ Myr}$ . All the relevant numbers describing the properties of the source and of

<sup>23</sup> All quantities relevant to the individual boxes are identified by an index  $i = 1, 12$  (e.g.,  $v_{\text{out},i}$ ) in order to distinguish them from the corresponding galaxy-integrated quantities (e.g.,  $v_{\text{out}}$ ).



**Table 3**  
Summary of Source and Outflow Properties

Source properties	
$L_{\text{TIR}(8-1000\ \mu\text{m})}$ [erg s <sup>-1</sup> ]	$2.71 \times 10^{45\text{a}}$
$L_{\text{Bol}}$ [erg s <sup>-1</sup> ]	$3.11 \times 10^{45\text{b}}$
$L_{\text{AGN}}$ [erg s <sup>-1</sup> ]	$(1.1 \pm 0.4) \times 10^{45\text{c}}$
$\alpha_{\text{AGN}} \equiv L_{\text{AGN}}/L_{\text{Bol}}$	$0.35 \pm 0.13$
SFR [ $M_{\odot}$ yr <sup>-1</sup> ]	$46 \pm 9^{\text{d}}$
$\dot{M}_{\text{mol}}^{\text{tot}}$ [ $M_{\odot}$ ]	$(2.1 \pm 0.5) \times 10^{10\text{e}}$
Molecular outflow properties (estimated in Section 3.4)	
$r_{\text{max}}$ [kpc]	$2.4 \pm 0.3^{\text{f}}$
$\langle v_{\text{out}} \rangle$ [km s <sup>-1</sup> ]	$250 \pm 50^{\text{g}}$
$\langle \sigma_{\text{out}} \rangle$ [km s <sup>-1</sup> ]	$220 \pm 20^{\text{g}}$
$\langle \tau_{\text{dyn}} \rangle$ [Myr]	$6.5 \pm 1.8^{\text{g}}$
$\dot{M}_{\text{out}}$ [ $M_{\odot}$ ]	$(1.2 \pm 0.3) \times 10^{10}$
$\dot{M}_{\text{out}}$ [ $M_{\odot}$ yr <sup>-1</sup> ]	$2500 \pm 1200$
$\nu \dot{M}_{\text{out}}$ [g cm s <sup>-2</sup> ]	$(3.1 \pm 1.2) \times 10^{36}$
$1/2\dot{M}_{\text{out}}v^2$ [erg s <sup>-1</sup> ]	$(3.6 \pm 1.6) \times 10^{43}$
$\eta \equiv \dot{M}_{\text{out}}/\text{SFR}$	$50 \pm 30$
$(\nu \dot{M}_{\text{out}})/(L_{\text{AGN}}/c)$	$80 \pm 50$
$(1/2\dot{M}_{\text{out}}v^2)/L_{\text{AGN}}$	$0.033 \pm 0.019$
$\tau_{\text{dep}} \equiv \dot{M}_{\text{mol}}^{\text{tot}}/\dot{M}_{\text{out}}$ [Myr]	$8 \pm 4$

#### Notes.

<sup>a</sup> From the *IRAS* Revised Bright Galaxy Sample (Sanders et al. 2003).

<sup>b</sup>  $L_{\text{Bol}} = 1.15 L_{\text{TIR}}$ , following Veilleux et al. (2009).

<sup>c</sup> Total bolometric luminosity of the dual AGN system estimated from X-ray data by Puccetti et al. (2016).

<sup>d</sup>  $\text{SFR} = (1 - \alpha_{\text{AGN}}) \times 10^{-10} L_{\text{TIR}}$ , following Sturm et al. (2011).

<sup>e</sup> Total molecular gas mass in the  $12'' \times 6''$  region encompassing the nucleus and the outflow, derived in Section 3.4.

<sup>f</sup> Maximum distance at which we detect [C I](1–0) in the outflow at a S/N > 3; hence the quoted  $r_{\text{max}}$  should be considered a lower limit constraint allowed by current data.

<sup>g</sup> Mean values obtained from the analysis of all boxes.

the molecular outflow are reported in Table 3 and will be discussed in Section 4.3 in the context of feedback models.

Very stringent lower limits on the outflow energetics can be derived by assuming that its CO(1–0) emission is fully optically thin. For optically thin gas and  $T_{\text{ex}} = 30$  K, the  $\alpha_{\text{CO}}$  factor would be  $\sim 0.34$  (Bolatto et al. 2013), and the outflow mass and mass-loss rate would be  $\dot{M}_{\text{out}} = (1.98 \pm 0.09) \times 10^9 M_{\odot}$  and  $d\dot{M}_{\text{out}}/dt = 430 \pm 160 M_{\odot} \text{ yr}^{-1}$ . However, we stress that the assumption of fully optically thin CO(1–0) emission in the outflow is not supported by our data, which instead favor an  $\alpha_{\text{CO}}$  factor for outflowing gas that is intermediate between the optically thin and the optically thick values (for solar metallicities).

### 3.5. Physical Properties of Quiescent and Outflowing Gas

Using the results of the spatially resolved analysis presented in Section 3.3, we now study how the  $\alpha_{\text{CO}}$  and  $r_{21}$  parameters vary as a function of velocity dispersion ( $\sigma_v$ ) and projected distance ( $d$ ) from the nucleus of NGC 6240. The relevant plots are shown in Figure 6. To investigate possible statistical correlations, we conduct a Bayesian linear regression analysis of the relations in Figure 6, following Kelly (2007).<sup>24</sup>

The left panels of Figure 6 do not indicate any statistically significant relation between  $\alpha_{\text{CO}}$  and either  $\sigma_v$  or  $d$ . Instead, they show that the  $\alpha_{\text{CO}}$  factor is systematically higher—although formally only at a significance of  $1.2\sigma$  (Table 2)—in the quiescent gas than in the outflow, regardless of the velocity dispersion of the clouds, or of their position with respect to the merger nucleus. For the *non-outflowing* components, the  $\alpha_{\text{CO}}$  factors are at least twice the so-called (U)LIRG value (Downes & Solomon 1998), and reach up to Galactic values. This result is consistent with the multi-transition analysis by Papadopoulos et al. (2014), and is likely due to the state of the dense gas phase that low- $J$  CO lines alone cannot constrain, but which instead is accounted for when using [C I](1–0) as a molecular mass tracer. Nevertheless, the *outflowing* H<sub>2</sub> gas has lower  $\alpha_{\text{CO}}$  values than the quiescent ISM. This is indeed expected from the ISM physics behind  $\alpha_{\text{CO}}$  for warm and strongly unbound gas states (Papadopoulos et al. 2012a)—that is, the type of gas that we expect to be embedded in outflows. In particular, in the case that molecular outflows are ubiquitous in (U)LIRGs, as suggested by observations (Sturm et al. 2011; Spoon et al. 2013; Veilleux et al. 2013; Cicone et al. 2014), the outflow may be the location of the diffuse and warm molecular gas phase that is not contained in self-gravitating cooler clouds—a sort of “intercloud” medium advocated by some of the previous analyses based solely on low- $J$  CO, <sup>13</sup>CO line observations (Aalto et al. 1995; Downes & Solomon 1998). Furthermore, the flat trend between  $\alpha_{\text{CO}}$  and  $d$  observed in Figure 6 does not support the hypothesis that the lower  $\alpha_{\text{CO}}$  values in (U)LIRGs are related to the collision of the progenitors’ disks, since in this case we would naively expect the lower  $\alpha_{\text{CO}}$  clouds to be concentrated in the central regions of the merger. The  $\alpha_{\text{CO}}$  values measured for the outflow components are, however, significantly higher than the optically thin value, suggesting that not all of the outflowing material is diffuse and warm, but there may still be a significant amount of dense gas. These results are further discussed and contextualized in Section 4.2.

The right panels of Figure 6 show a weak correlation between the  $r_{21}$  and  $\sigma_v$  (correlation coefficient,  $\rho = 0.4 \pm 0.2$ ) and an anti-correlation with the distance, although only for the systemic/quiescent components ( $\rho = -0.7 \pm 0.2$ ). The corresponding best fit relations, of the form  $r_{21} = \alpha + \beta x$ , plotted in Figure 6, have  $(\alpha, \beta) = (0.8 \pm 0.2, 2.1 \pm 1.4 \times 10^{-3})$  for  $x = \sigma_v$ , and  $(\alpha, \beta) = (1.5 \pm 0.2, -0.33 \pm 0.13)$  for  $x = d$ . The systemic ISM shows  $0.8 \lesssim r_{21} \lesssim 1.4$ , whereas the outflow is characterized by higher ratios, with most components in the range  $1.2 \lesssim r_{21} \lesssim 2.5$ , although we observe a large spread in  $r_{21}$  values at  $d > 2$  kpc.

CO(2–1)/CO(1–0) luminosity ratios of  $r_{21} \sim 0.8$ –1.0 are typically found in the molecular disks of normal spiral galaxies (Leroy et al. 2009) and are indicative of optically thick CO emission with  $T_{\text{kin}} \sim 10$ –30 K (under LTE assumptions). Nevertheless, such low- $J$  CO line ratios, in absence of additional transitions, are well-known to be highly degenerate tracers of the average gas physical conditions. Higher- $J$  data of CO, molecules with larger dipole moment, and isotopologues can break such degeneracies. Such studies exist for NGC 6240 (Greve et al. 2009; Meijerink et al. 2013; Papadopoulos et al. 2014), and found extraordinary states for the molecular gas, with average densities typically above  $10^4 \text{ cm}^{-3}$  and temperatures  $T_{\text{kin}} \sim 30$ –100 K.

<sup>24</sup> We used the IDL routine `linmix_err.pro`.

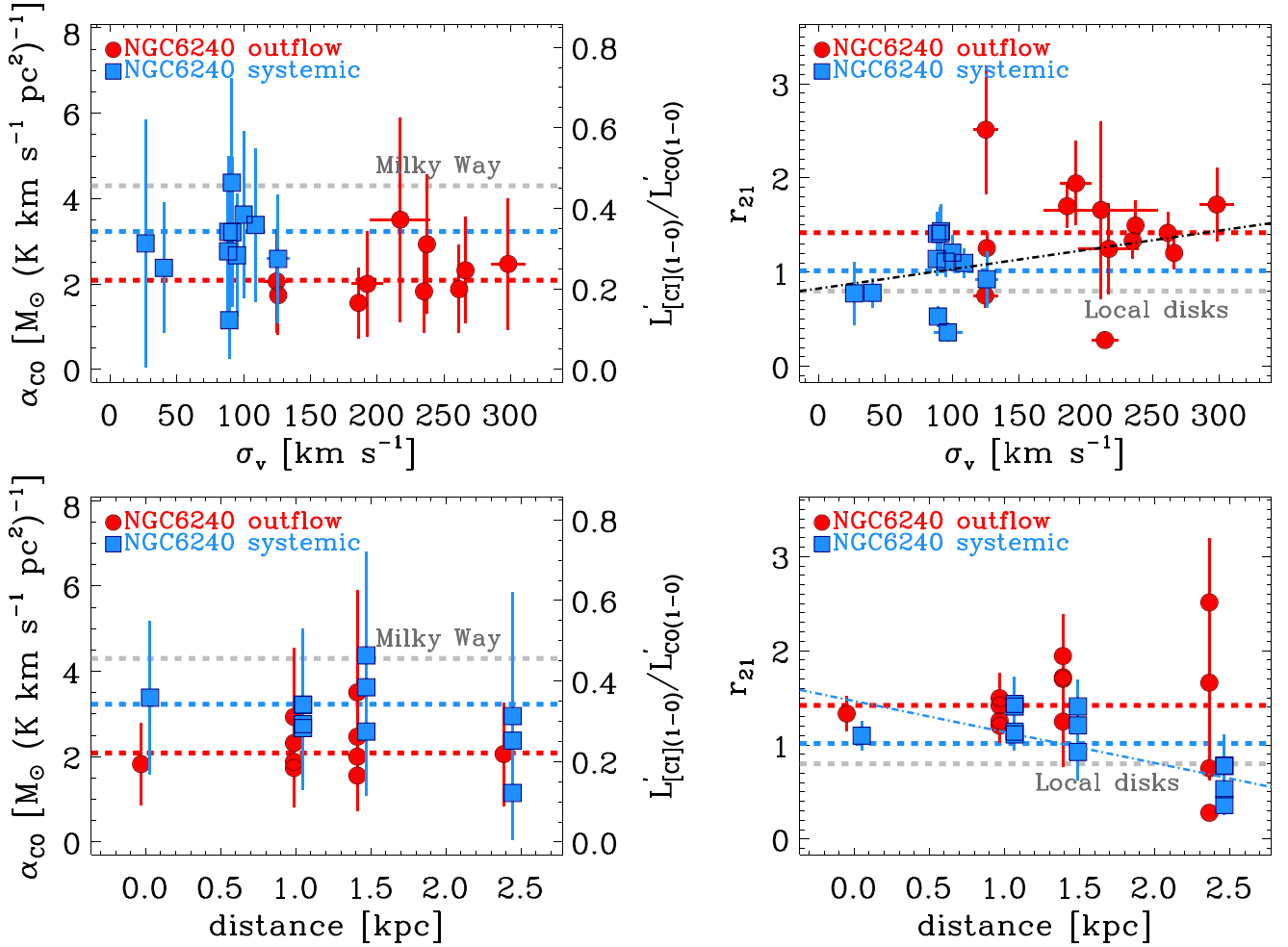


**Figure 6.**  $\alpha_{\text{CO}}$  (left) and  $r_{21}$  (right) as a function of the average velocity dispersion (top) and of the distance from the nucleus (bottom) of the corresponding molecular line components. A detailed explanation on how  $\alpha_{\text{CO}}$  and  $r_{21}$  were calculated can be found in Section 3.3. The y-axis on the right side of the  $\alpha_{\text{CO}}$  plots shows the corresponding [C I](1–0)/CO(1–0) line luminosity ratio. The horizontal blue and red dashed lines are the mean values reported in Table 2 for the systemic and outflow components, respectively. The gray lines indicate the Milky Way  $\alpha_{\text{CO}}$  factor (Bolatto et al. 2013, left panels) and the average  $r_{21} = 0.8$  measured in star-forming galaxies (Leroy et al. 2009, right panels). The best fits obtained from a Bayesian linear regression analysis following the method by Kelly (2007) are plotted using dot-dashed lines: black lines show the best fits to the total sample, whereas blue and red lines correspond to the fits performed separately on the systemic and outflowing components.

On the contrary, global CO(2–1)/CO(1–0) ratios exceeding unity have a lower degree of degeneracy in terms of the extraordinary conditions that they imply for molecular gas, as they require warmer ( $T_{\text{kin}} \gtrsim 100$  K) and/or strongly unbound states (Papadopoulos et al. 2012b). In NGC 6240, optical depth effects are most likely at the origin of the  $r_{21} > 1$  values. More specifically, such ratios can result from highly non-virial motions (e.g., the large velocity gradients of the outflowing clouds), causing the CO lines to become partially transparent, as also supported by the tentative trend of increasing  $r_{21}$  with  $\sigma_v$  (Figure 6). This finding independently strengthens our explanation for the lower  $\alpha_{\text{CO}}$  factors derived for the outflowing gas, which are intermediate between an optically thin and an optically thick value (for typical solar CO abundances).

## 4. Discussion

### 4.1. Assumptions and Caveats of Our Analysis

Our results build, on the one hand, on the identification of the outflow components, and on the other hand on the assumption that CO(1–0) and [C I](1–0) trace the same

molecular gas, implying that  $M_{\text{mol}}$  can be measured from [C I](1–0). In this section we further comment on these steps and discuss their caveats and limitations.

#### 4.1.1. The Outflow Identification

The outflow identification is a fundamental step of our analysis, and leads to one of our most surprising findings: that  $60 \pm 20\%$  of the molecular ISM in NGC 6240 belongs to the outflow. This unprecedented result may hold the key to finally understanding the extreme ISM of this source, which makes it an outlier even compared to other (U)LIRGs, as acknowledged by several authors (Meijerink et al. 2013; Papadopoulos et al. 2014; Israel et al. 2015). For example, Meijerink et al. (2013) suggested that the CO line emission in NGC 6240 is dominated by gas settling down after shocks, which would be consistent with gas cooling out of an outflow. A massive outflow would also explain why the gaseous and stellar kinematics are decoupled (Tacconi et al. 1999; Engel et al. 2010).

In Section 3.3 we have ascribed to the outflow all spectral line components with  $\text{FWHM} > 400 \text{ km s}^{-1}$ ,  $v < -200 \text{ km s}^{-1}$ , or  $v > +250 \text{ km s}^{-1}$  detected within the central  $12'' \times 6''$  region

investigated in this paper. However, the spatial information is also crucial for identifying outflowing gas, especially in a source undergoing a major merger, since the outflow signatures may be degenerate with gravity-driven dynamical effects. In the specific case of NGC 6240, as explained later and shown in detail in Appendix B, the high S/N and spatial resolution of our observations allow us to disentangle feedback-related effects from other mechanisms and reliably identify the outflow emission.

During a galaxy collision, high- $v$ /high- $\sigma_v$  gas can be concentrated in the nuclear region as a consequence of gravitational torques, which cause a fraction of the gas to lose angular momentum and flow toward the center. At the same time, gravitational torques and tidal forces can drive out part of the gas from the progenitors' disks and form large-scale filaments denominated "tidal tails" and "bridges." However, in the case of NGC 6240, these gravity-induced mechanisms can hardly explain the kinematics and morphology of the  $\sim 10$  kpc-scale, wide opening angle-emission shown in Figures 1–3. In particular, the high- $v$ /high- $\sigma_v$  structures revealed by the [C I] (1–0) moment maps, which are correlated with features observed on much larger scales (see Section 3.1), cannot be due to nuclear inflows. In this case, we would indeed expect the  $\sigma_v$  of the gas to be enhanced toward the nucleus (or nuclei), rather than in offset positions that are several 100s of pc away from the nuclei or from the geometric center of the AGN pair (see, for example, the different signature of outflows and inflows in the velocity dispersion maps shown by Davies et al. 2014). The hourglass-shaped configuration visible in the [C I](1–0) velocity dispersion map is more suggestive of an outflow opening toward east and west (i.e., along the same directions of expansion of the high- $v$  gas).

On larger scales, tidal tails or bridges produced in galaxy collisions may also affect the dynamical state of the ISM. However, the line-widths of the molecular emission from such filamentary structures are rather low ( $\sim 50$ – $100$  km s $^{-1}$ , Braine et al. 2001). Therefore, in order to reproduce the spatially and kinematically coherent structure shown in Figures 1, and especially the spatial overlap across several kpc between the highly blueshifted and redshifted emissions (Figure 2), one would need to postulate a very specific geometry where several tidal tails overlap along the line of sight across more than 10 kpc.

Based on these considerations, and on the detailed discussion reported in Appendix B, we conclude that other mechanisms such as rotating disks or gravity-induced dynamical motions, possibly also coexisting in NGC 6240, are unlikely to significantly affect our outflow energetics estimates.

#### 4.1.2. Combining [C I](1–0) and CO(1–0) Data to Infer $\alpha_{\text{CO}}$ and $M_{\text{mol}}$

The second key step of our analysis is to combine the [C I] (1–0) and CO(1–0) line observations to derive molecular gas masses. As described in Sections 3.2–3.4, our strategy is to use the places where [C I](1–0) and CO(1–0) are both detected at a  $S/N \geq 3$  to measure the corresponding  $\alpha_{\text{CO}}$ . Molecular gas masses are then computed by using the CO(1–0) data. In particular, we select components where CO(1–0) is detected at a  $S/N \geq 3$  and convert  $L'_{\text{CO}(1-0)}$  into  $M_{\text{mol}}$  by employing either the corresponding [C I]-derived  $\alpha_{\text{CO}}$  (possible only if [C I] (1–0) is also detected with  $S/N \geq 3$ ) or alternatively by using the mean  $\alpha_{\text{CO}}$  value appropriate for that component (i.e., "global," "systemic," or "outflow"; Table 2).

The fundamental underlying assumption is that [C I] (1–0) and CO(1–0) trace the same material. Earlier theoretical works envisioned neutral carbon to be confined in the external (low extinction  $A_V$ ) layers of molecular clouds—hence to probe a different volume compared to CO. However, as discussed by Papadopoulos et al. (2004), this theory was dismantled by observations finding a very good correlation between [C I] and CO as well as uniform [C I]/CO ratios across a wide range of Galactic environments, including regions shielded from FUV photons (e.g., Keene et al. 1985; Ojha et al. 2001; Tanaka et al. 2011). The few available observations of [C I] lines in local galaxies have further supported the concurrence of CO and [C I] in different physical conditions (Israel et al. 2015; Krips et al. 2016).

The good mixing of CO and [C I] could be a consequence of turbulence and/or CRs. Turbulent diffusion can merge any [C I]-rich H $_2$  phase (expected to prevail in low  $A_V$  regions) with the more internal CO-rich H $_2$  gas, hence uniforming the [C I]/CO abundance ratio throughout molecular clouds (Glover et al. 2015). CRs, by penetrating deep into molecular clouds and so destroying CO (but not H $_2$ ) over larger volumes compared to FUV photons, can also help enrich the internal regions of clouds with neutral carbon (Bisbas et al. 2015, 2017). Both mechanisms are expected to be efficient in (U)LIRGs and in their molecular outflows. The latter are (by definition) highly turbulent environments. Furthermore, CRs originating in the starburst nuclei can leak along such outflows, hence influencing the chemistry of their embedded ISM (see the discussion in Papadopoulos et al. 2018, and recent results by González-Alfonso et al. 2018). For these reasons, we can assume that CO and [C I] trace the same molecular gas, for both the quiescent and outflowing components of NGC 6240.

Thanks to the simple three-level partition function of neutral carbon, and to its lines being optically thin in most cases (including NGC 6240, Israel et al. 2015), the main sources of uncertainties for [C I]-based mass estimates are  $X_{\text{C I}}$  and  $T_{\text{ex}}$  (Equation (1)). Previous observations indicate very little variations in  $X_{\text{C I}}$  in the metal-enriched ISM of IR-luminous galaxies at different redshifts (Weiß et al. 2003, 2005; Danielson et al. 2011; Alaghband-Zadeh et al. 2013), including the extended ( $r > 10$  kpc) circumgalactic medium of the Spiderweb galaxy (Emonts et al. 2018). In our calculations we assumed  $X_{\text{C I}} = (3.0 \pm 1.5) \times 10^{-5}$  to take into account a systematic uncertainty associated with the [C I]/H $_2$  abundance ratio. Because of the particular LTE partition function of neutral carbon, [C I]-derived masses depend little on  $T_{\text{ex}}$  for  $T_{\text{ex}} \gtrsim 15$  K. We set  $T_{\text{ex}} = 30$  K, which is consistent with the value that can be estimated from the global [C I]2–1/1–0 brightness temperature ratio measured in NGC 6240 (Papadopoulos et al. 2014).

Therefore, our assumptions regarding the conversion between [C I](1–0) line data and  $M_{\text{mol}}$  are well justified by previous results. However, we caution that a giant galactic-scale outflow such as the one hosted by NGC 6240 constitutes an unprecedented environment for molecular gas clouds, and there is no comparable laboratory in our Galaxy that can be used as a reliable reference. The study of the physical conditions of such outflows has only just started, and this is the first time that the [C I](1–0) line emission from high-velocity gas components extending by several kpc has been imaged at high spatial resolution. Further investigation is needed, and our work constitutes just a starting point.



#### 4.2. The Role of Outflows in the Global $\alpha_{\text{CO}}$ Factor

The average  $\alpha_{\text{CO}}$  factors that we measure for the quiescent and outflowing components of the ISM in NGC 6240 (Table 2) are both higher than the classic (U)LIRG  $\alpha_{\text{CO}}$ . How can we reconcile this result with previous works advocating for significantly lower  $\alpha_{\text{CO}}$  values in (U)LIRGs? In the case of NGC 6240, our analysis has highlighted several effects that may have plagued previous  $\alpha_{\text{CO}}$  estimates:

1. The widespread presence of outflowing gas implies that, at any location within this merger, the molecular line emission includes a significant contribution from the outflow, with its overall lower  $\alpha_{\text{CO}}$  and higher  $r_{21}$ . As a result, an analysis of the global ISM conditions (especially if based only on low- $J$  CO lines; see also point 3 of this list) would get contaminated by the warm unbound  $\text{H}_2$  envelopes in the outflow, and their larger  $L'_{\text{CO}}/M_{\text{H}_2}$  ratios would drive down the global  $\alpha_{\text{CO}}$  estimate (Yao et al. 2003; Papadopoulos et al. 2012a).
2. The outflow dominates the velocity field of the  $\text{H}_2$  gas throughout the entire source, including the central region (Figure 3). The apparent nuclear north–south velocity gradient identified in previous CO line data (Bryant & Scoville 1999; Tacconi et al. 1999) is actually not compatible with ordered rotation once observed at higher spatial resolution, but it shows several features distinctive of the outflow. Therefore, the assumption that the molecular gas in this area is dominated by ordered motions is broken, making any dynamical mass estimate unreliable (if the outflow is not properly taken into account).
3. Previous analyses based only on low- $J$  CO lines have probably missed a substantial fraction of the denser gas phase that is instead accounted for when using the optically thin [C I](1–0) line as a gas mass tracer, or when probing the excitation of the ISM using high- $J$  CO transitions and high density molecular gas tracers. Indeed, the  $\alpha_{\text{CO}}$  value derived for the quiescent gas reservoir is consistent with a significant contribution from a dense gas state. Even in the outflow, the average  $\alpha_{\text{CO}}$  is still significantly higher than the optically thin value; hence the presence of dense gas may not be negligible. A conspicuous dense gas phase has already been demonstrated in a few other galaxy-wide molecular outflows (Aalto et al. 2012; García-Burillo et al. 2014; Sakamoto et al. 2014; Alatalo et al. 2015), and its presence would make more likely the formation of stars within these outflows (Maiolino et al. 2017).
4. The molecular gas emission in NGC 6240 is clearly very extended—both spectrally and spatially. As a result, at least some of the previous interferometric observations (especially “pre ALMA”) may have been severely affected by incomplete  $uv$  coverages filtering out the emission on larger scales, hence impacting on the measured line fluxes and sizes. Furthermore, as already noted by Tacconi et al. (1999), an insufficient spectral bandwidth may have hindered a correct baseline and/or continuum fitting and subtraction. The latter can be an issue for both single-dish and interferometric observations, including observations with ALMA if only one spectral window is employed to sample the line.

Since molecular outflows are a common phenomenon in local (U)LIRGs (Sturm et al. 2011; Spoon et al. 2013; Veilleux et al. 2013; Cicone et al. 2014; Fluetsch et al. 2018), at least some of the previously listed considerations may be generalized to their entire class. Therefore, it is possible that the so-called (U)LIRG  $\alpha_{\text{CO}}$  factor is an artifact resulting from modeling the molecular ISM of such sources containing massive  $\text{H}_2$  outflows.

#### 4.3. An Interplay of Feedback Mechanisms at Work

The extreme spatial extent of its molecular outflow makes NGC 6240 one of the few sources—all powerful quasars—hosting  $\text{H}_2$  outflows with sizes of  $\gtrsim 10$  kpc (Veilleux et al. 2017; see also the 30 kpc size [C II] $\lambda 158 \mu\text{m}$  outflow at  $z = 6.4$  studied by Cicone et al. 2015). In comparison, the  $\text{H}_2$  gas entrained in the well-studied starburst-driven winds of M82 and NGC 253 reaches maximum scales of  $\sim 1$ – $2$  kpc (Walter et al. 2002, 2017). Furthermore, among all the large-scale molecular outflows discovered so far in quasar host galaxies, the outflow of NGC 6240 is the one that has been observed at the highest spatial resolution ( $\sim 120$  pc). Indeed, the ALMA [C I](1–0) line data allowed us to probe deep into the nuclear region of the merger, close to the launching point of the molecular wind, and surprisingly revealed that the outflow emission peaks between the two AGNs rather than on either of the two. This is apparently at odds with an AGN radiative-mode feedback scenario, in which the multiphase outflow is expected to be generated close to the central engine (Costa et al. 2015).

Nevertheless, the role of the AGN(s) is certified by the extreme energetics of the molecular outflow, which have been constrained here with unprecedented accuracy. By comparing our  $\dot{M}_{\text{out}}$  and  $\dot{M}_{\text{mol}}^{\text{tot}}$  estimates (Table 3), it appears that  $60 \pm 20\%$  of the molecular medium is involved in the outflow. The estimated mass-loss rate of  $2500 \pm 1200 M_{\odot} \text{ yr}^{-1}$  corresponds to  $\eta \equiv \dot{M}_{\text{out}}/\text{SFR} = 50 \pm 30$ , whereas the lower limit on  $\dot{M}_{\text{out}}$ , calculated using the optically thin  $\alpha_{\text{CO}}$  prescription, corresponds to  $\eta \equiv \dot{M}_{\text{out}}/\text{SFR} = 9 \pm 4$ . Such high mass loading factors are inconsistent with a purely star formation-driven wind. As a matter of fact, stellar feedback alone can hardly bear outflows with  $\eta$  much higher than unity. Cosmological hydrodynamical simulations incorporating realistic stellar feedback physics, by including mechanisms other than supernovae, can reach up to  $\eta \sim 10$  (Hopkins et al. 2012). However, because  $\eta$  in these simulations anti-correlates with the mass of the galaxy, the highest  $\eta$  values are generally predicted for dwarf galaxies, whereas for galaxies with baryonic masses of several  $10^{10} M_{\odot}$  such as NGC 6240, the  $\eta$  achievable by stellar feedback can be at maximum 2–3.

Based on its energetics, we can therefore rule out that the massive molecular outflow observed in NGC 6240 is the result of star formation alone. The outflow energetics can instead be fully accommodated within the predictions of AGN feedback models (Faucher-Giguère & Quataert 2012; Costa et al. 2014; Zubovas & King 2014). In addition, these models can explain the multi-wavelength properties of NGC 6240. At optical wavelengths, NGC 6240 is known to host a ionized wind (Heckman et al. 1990), with large-scale superbubbles expanding by tens of kpc toward north–west and south–east (Veilleux et al. 2003; Yoshida et al. 2016). The  $\text{H}\alpha$  emission from the ionized wind shows a close spatial correspondence with the soft X-ray continuum, suggesting the presence of gas cooling out of a shocked medium (Nardini et al. 2013). Furthermore,

Wang et al. (2014) detected a diffuse component in hard-X-ray continuum and Fe XXV line emission, tracing  $T \sim 7 \times 10^7$  K gas between the two AGNs (north–west of the southern nucleus, similar to the [C I](1–0) blue wing in Figure 1(d)), as well as in kpc-scale structures that are remarkably coincident with both the strong NIR  $H_2$  emission (van der Werf et al. 1993; Max et al. 2005) and the  $H\alpha$  filaments.

At radio wavelengths, Colbert et al. (1994) reported the detection of non-thermal continuum emission with a steep spectrum extending by several kpc in an arclike structure west of the AGNs, later confirmed also by Baan et al. (2007), together with a possibly similar feature on the eastern side. This structure lacks a clear spatial correspondence with optical or NIR starlight (which excludes a starburst origin), and its complex morphology suggests a connection with the  $H\alpha$  outflow. Theoretically, the association between an AGN-driven wind and extended non-thermal radiation (due to relativistic electrons accelerated by the forward shock) has been predicted by Nims et al. (2015). Observationally, the rough alignment of the western arclike structure discovered by Colbert et al. (1994) with the molecular outflow studied in this work would also support this hypothesis, although the current data do not allow us to probe the presence of  $H_2$  outflowing gas at the exact position of the radio emission. The total radio power of this arclike feature is comparable with that of extended radio structures previously observed in radio-quiet AGNs with prominent outflows (Morganti et al. 2016). Future facilities like the Cherenkov Telescope Array may reveal the  $\gamma$ -ray counterpart of the non-thermal emission, as expected for an AGN outflow shock (Lamastra et al. 2017).

In summary, all these multi-wavelength observational evidences point to a radiative-mode AGN feedback mechanism (Faucher-Giguère & Quataert 2012; Nims et al. 2015). However, at the same time, it is difficult to reconcile a classic model with an  $H_2$  outflow whose emission does not peak on either of the two AGNs. A complex interplay of stellar and AGN feedback must be at work in this source (see also Müller-Sánchez et al. 2018), and we cannot exclude the additional contribution from compact radio-jets (Gallimore & Beswick 2004), which may be accelerating part of the cold material (Mukherjee et al. 2016). Finally, positive feedback may also be at work in NGC 6240. There is indeed a striking correspondence between (1) the morphology of the approaching side of the outflow north–west of the southern AGN (Figure 1(d)), (2) a peak of dust extinction, and (3) a stellar population with unusually large stellar  $\sigma_v$  and blueshifted velocities (Engel et al. 2010). The latter, according to Engel et al. (2010), may have been formed recently as a result of crushing of molecular clouds, which could be related to the observed outflow event (Zubovas & King 2014; Maiolino et al. 2017), provided these stars are not older than a few Myr.

## 5. Summary and Conclusions

A powerful multiphase outflow shapes the distribution of gas in NGC 6240, and it is likely at the origin of many of the extraordinary features that for years have puzzled scientists studying this source. In this work we used new ALMA [C I](1–0) line observations, in combination with ALMA CO(2–1) and IRAM PdBI CO(1–0) line data, to study the morphology, energetics, and physical state of the molecular component of the outflow. Our main findings are as follows.

1. The molecular outflow extends by more than 10 kpc along the east–west direction, and it is clearly detected in both its approaching (blueshifted) and receding (redshifted) sides. Its emission peaks between the two AGNs, rather than on either of the two. Furthermore, the outflow dominates the  $H_2$  gas velocity field in the merger nucleus, as shown by the presence of a striking hourglass-shaped feature in the high-res ( $\sim 0''.24$ ) [C I](1–0) line moment 2 map. This high- $\sigma_v$  structure, aligned east–west, traces the launch base of the kpc-scale outflow. The outflow, with its large flux contribution to the molecular line emission in the nucleus, can explain both the high gas turbulence and the strong decoupling of stellar and gaseous kinematics evidenced in this source by previous works.
2. We combined the [C I](1–0) and CO(1–0) line observations to derive the  $\alpha_{CO}$  factor in the outflow, which is on average  $\langle \alpha_{CO} \rangle = 2.1 \pm 1.2 M_\odot (\text{K km s}^{-1} \text{pc}^2)^{-1}$ . The information on the  $\alpha_{CO}$ , in conjunction with a spatially resolved spectral analysis of the molecular line emission, allowed us to constrain with unprecedented accuracy the energetics of the molecular outflow. We estimate that the outflow entrains  $\dot{M}_{out} = (1.2 \pm 0.3) \times 10^{10} M_\odot$ , corresponding to  $60 \pm 20\%$  of the molecular reservoir of NGC 6240. The total mass-loss rate is  $\dot{M}_{out} = 2500 \pm 1200 M_\odot \text{ yr}^{-1} = 50 \pm 30 \text{ SFR}$ , which energetically rules out a solely star formation-driven wind.
3. For the quiescent gas components, the  $\alpha_{CO}$  factors are on average higher than in the outflow (irrespective of their distance from the nucleus), with a mean value of  $\langle \alpha_{CO} \rangle = 3.2 \pm 1.8 M_\odot (\text{K km s}^{-1} \text{pc}^2)^{-1}$ —that is, at least twice the so-called (U)LIRG value. This result is consistent with recent multi-transition ISM analyses and is likely due to a dense gas phase that cannot be constrained by using low- $J$  CO lines alone, but which is instead accounted for when using [C I](1–0) as a molecular gas tracer.
4. We observe a tentative trend of increasing  $r_{21}$  ratios with  $\sigma_v$  and measure  $r_{21} > 1$  values in the outflow ( $\langle r_{21} \rangle = 1.4 \pm 0.3$ ), while  $r_{21} \simeq 1$  for quiescent gas. We explain the  $r_{21} > 1$  ratios with optical depth effects, whereby the highly non-virial motions of the outflowing clouds cause the CO lines to become partially transparent.
5. Based on the finding that lower  $\alpha_{CO}$  and higher  $r_{21}$  values are typical of the outflowing clouds, we propose that molecular outflows are the location of the warm and strongly unbound phase—the “intercloud medium” invoked by previous studies—that drives down the global  $\alpha_{CO}$  in (U)LIRGs. However, we note that the [C I]-based  $\alpha_{CO}$  factor derived for the outflow is higher than the optically thin value, suggesting that not all of the outflowing material is in such warm diffuse phase but that there may still be a significant amount of dense gas entrained.
6. The outflow kinetic power and momentum rate, respectively equal to  $(0.033 \pm 0.019) L_{AGN}$  and  $(80 \pm 50) L_{AGN}/c$ , could be fully accommodated within the predictions of AGN “blast-wave” feedback models. However, the puzzling outflow morphology, with a launch region situated between the two AGNs, and a direction of expansion perpendicular to the axis connecting the two nuclei, challenges a classic AGN

feedback scenario. A complex interplay of stellar and AGN feedback processes must be at work in NGC 6240.

This project has received funding from the European Union’s Horizon 2020 research and innovation programme under the Marie Skłodowska-Curie grant agreement No 664931. The research leading to these results has received funding from the European Union’s Horizon 2020 research and innovation programme under grant agreement No 730562 [RadioNet]. R.M. acknowledges ERC Advanced Grant 695671 “QUENCH” and support by the Science and Technology Facilities Council (STFC). E.T. acknowledges support from FONDECYT regular grant 1160999 and Basal-CATA PFB-06/2007. G.C.P. acknowledges support from the University of Florida. We thank the referee for his/her constructive report, which helped us improve the discussion of the results. This paper makes use of the following ALMA data: ADS/JAO. ALMA #2015.1.00717.S and #2015.1.00370.S. ALMA is a partnership of ESO (representing its member states), NSF (USA), and NINS (Japan), together with NRC (Canada), MOST and ASIAA (Taiwan), and KASI (Republic of Korea), in cooperation with the Republic of Chile. The Joint ALMA Observatory is operated by ESO, AUI/NRAO, and NAOJ. This publication makes use of observations carried out with the IRAM Plateau de Bure Interferometer. IRAM is supported by INSU/CNRS (France), MPG (Germany), and IGN (Spain). C.C. thanks Sandra Burkutean for helping her with the combination of the ALMA and ACA B8 data cubes and Alvaro Hacar Gonzalez for suggesting to use the ACA B8 data as a source model in the cleaning of the ALMA B8 data cubes, which significantly improved the results.

*Facilities:* ALMA, IRAM PdBI.

*Software:* CASA v4.6.0, GILDAS (Pety 2005).

## Appendix A

### Additional CO(1–0) and CO(2–1) Outflow Maps

Interferometric maps of the CO(1–0) and CO(2–1) high-velocity emissions are shown in Figure 7 separately for the blue (left panels: a, c) and red (right panels: b, d) line wings. To produce these maps, the CO(1–0) and CO(2–1)  $uv$  visibilities have been integrated within the same velocity ranges as in Figure 1. Figure 7 demonstrates that the blue and red wings of the low- $J$  CO lines in NGC 6240 are both spatially extended on scales of several kpc, with their most extended features aligned preferentially along the east–west direction. The positive contours of the CO(2–1) blue and red line wing emissions shown in Figures 7(c), (d) are overplotted in Figure 2 to allow a direct comparison of their extent and morphology.

## Appendix B

### Box Spectra and Outflow Identification

The CO(1–0), CO(2–1), and [C I](1–0) box spectra extracted from the grid shown in panel (a) of Figure 1 are presented in Figures 8–10. The results of the simultaneous fitting procedure described in Section 3.3 are overplotted on the data. Each spectrum is labeled with the box ID: IDs C1–C9 correspond to the central  $2'' \times 2''$  boxes, whereas E1–E2 and W1–W2 are respectively the eastern and western  $3'' \times 3''$  boxes. The spectral components resulting from the simultaneous fit are classified as “outflow” or “quiescent” according to their

velocity shift and dispersion, as described in Section 3.3. In the following, we examine—case by case—the results of such outflow identification procedure (see also Section 4.1.1 for a more general discussion).

It is already evident from Figures 1(a)–(c) that the bulk of the molecular line emission at high projected velocities traces a very extended, non-collimated structure aligned east–west, with a large overlap between the blue and redshifted sides (Figure 2). As best seen in the high S/N CO(2–1) spectra in Figure 9, the boxes E1, E2, W1, and W2, tracing gas at  $d > 2$  kpc from the nucleus, exhibit broad spectral features—distinguishable from the narrow components—which in some cases (e.g., E1) dominate the total CO flux. Such broad wings are characterized by velocity shifts ( $v \sim 300$ – $600$  km s $^{-1}$ ) and dispersions ( $\sigma_v \sim 125$ – $215$  km s $^{-1}$ ) that are much higher than the narrow components detected in the same spectra ( $v \sim 30$ – $180$  km s $^{-1}$ ,  $\sigma_v \sim 30$ – $100$  km s $^{-1}$ ). As a result, we identify the high- $v$ , high- $\sigma_v$  spectral components at  $d > 2$  kpc as due to an outflow.

Closer to the nucleus, the outflow identification becomes more challenging. However, once we have identified the broad components in E1, E2, W1, W2 as part of an outflow, then it is natural to ascribe similar broad components—spatially aligned along the east–west axis—to the same outflow. In particular, C4 and C8 (east and west of the nucleus), C2–C3 (north–west of the nucleus, along the same direction as the high- $v$  structure in Figure 1(e)), and C6–C7 (south–east of the nucleus, along another direction of outflow expansion as shown in Figure 1(d)) also show a broad component extending up to  $\sim 1000$  km s $^{-1}$  on both the red and blueshifted sides. The outflow identification is more uncertain for boxes C5 and C9, where the wings are less prominent than in other regions, and the spatial alignment with the larger-scale outflow is not obvious. However, the contribution from these boxes to the total outflow mass and mass-loss rate is negligible. Indeed, without C5 and C9, we derive  $M_{\text{out}} = 1.1 \times 10^{10} M_{\odot}$  and  $dM_{\text{out}}/dt = 2350 M_{\odot} \text{ yr}^{-1}$ , consistent with the values given in Table 3. Hence the uncertain outflow identification in boxes C5 and C9 does not affect our results.

We now discuss the central box C1, which alone contributes to  $M_{\text{out}}^{\text{C1}} = (4 \pm 2) \times 10^9 M_{\odot}$  and  $dM_{\text{out}}^{\text{C1}}/dt = 1400 \pm 1100 M_{\odot} \text{ yr}^{-1}$ . There are several arguments in support of a significant outflow contribution in this region: (1) there is a striking similarity between the C1 spectrum with that of the adjacent box C8; (2) there is a notion that the outflow must originate from within this region because it hosts two AGNs and most of the star formation activity; (3) the [C I](1–0) emission at  $|v| > 200$  km s $^{-1}$  arising from within this region is spatially extended and follows the morphology of the larger-scale outflow (Figures 1(d), (e)); (4) in this region, the outflow dominates even the emission at low projected velocities, as shown by Figure 3; (5) the  $\alpha_{\text{CO}}$  and  $r_{21}$  values calculated for the outflow components identified in box C1 (data points at  $d = 0$  kpc in the bottom panels of Figure 6) are consistent with the values measured in the larger-scale outflow.

Therefore, based on the spectral and spatial properties of the molecular line emission that we have ascribed to the outflow, we conclude that alternative mechanisms such as rotating disks and tidal tails are unlikely to significantly affect our outflow energetics estimates.



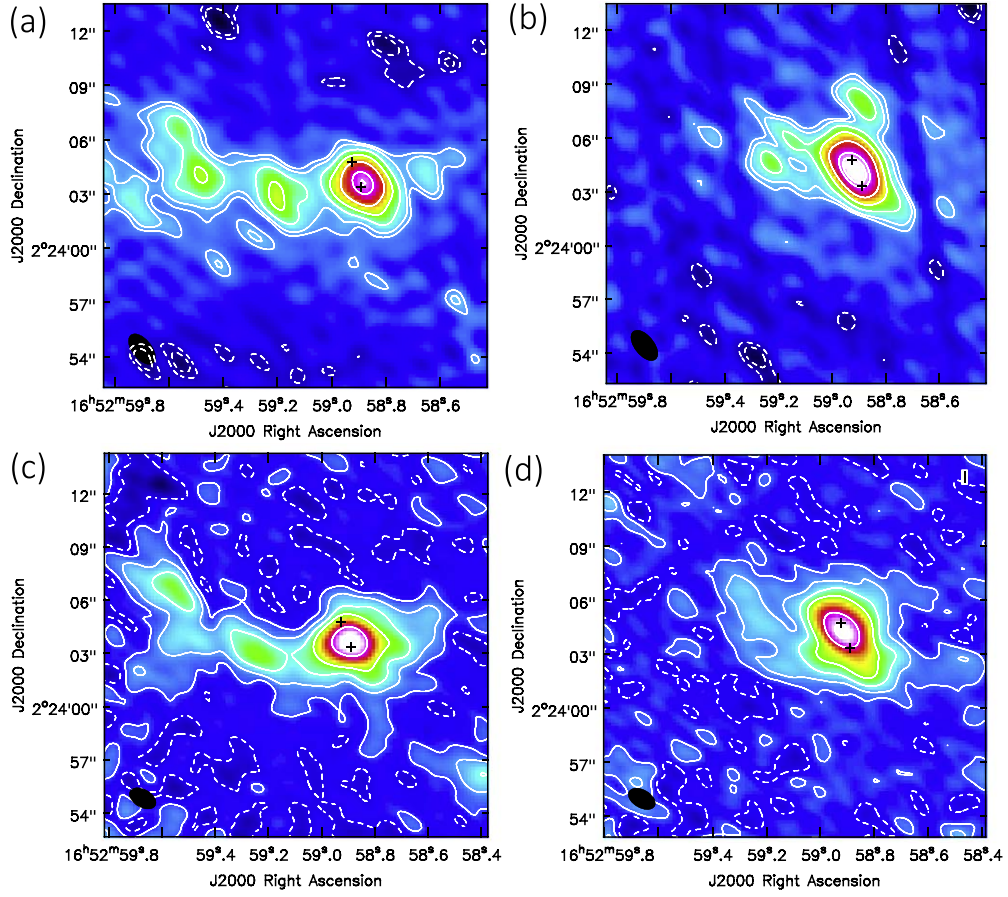


**Figure 7.** CO(1–0) (top row) and CO(2–1) (bottom row) interferometric maps of the outflow emission, integrated in the blue (a, c) and red (b, d) wings, by using the same velocity ranges as in Figure 1. The maps have matched spatial resolution ( $\sim 1''/2$ , details in Section 2). Contours correspond to  $(-3\sigma, -2\sigma, 2\sigma, 3\sigma, 6\sigma, 12\sigma, 24\sigma, 48\sigma, 60\sigma)$  with  $1\sigma = 0.33 \text{ mJy beam}^{-1}$  in panel (a) and  $1\sigma = 0.39 \text{ mJy beam}^{-1}$  in panel (b);  $(-3\sigma, 3\sigma, 10\sigma, 24\sigma, 48\sigma, 200\sigma, 350\sigma)$  with  $1\sigma = 0.33 \text{ mJy beam}^{-1}$  in panel (c) and  $1\sigma = 0.3 \text{ mJy beam}^{-1}$  in panel (d). Similar to Figure 1, the black crosses indicate the VLBI positions of the AGNs from Hagiwara et al. (2011).

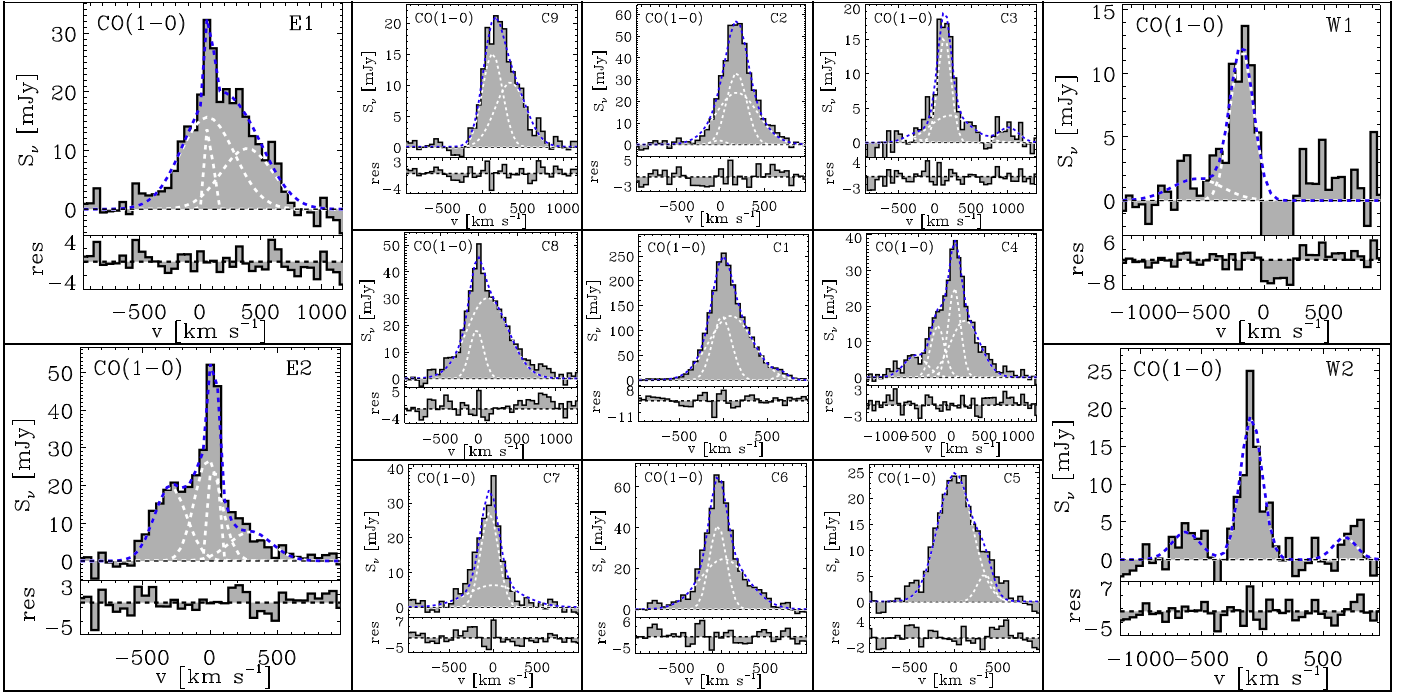


Figure 8. CO(1-0) spectra extracted from the grid of 13 boxes shown in panel (a) of Figure 1, with overplotted the results of the simultaneous fit procedure.

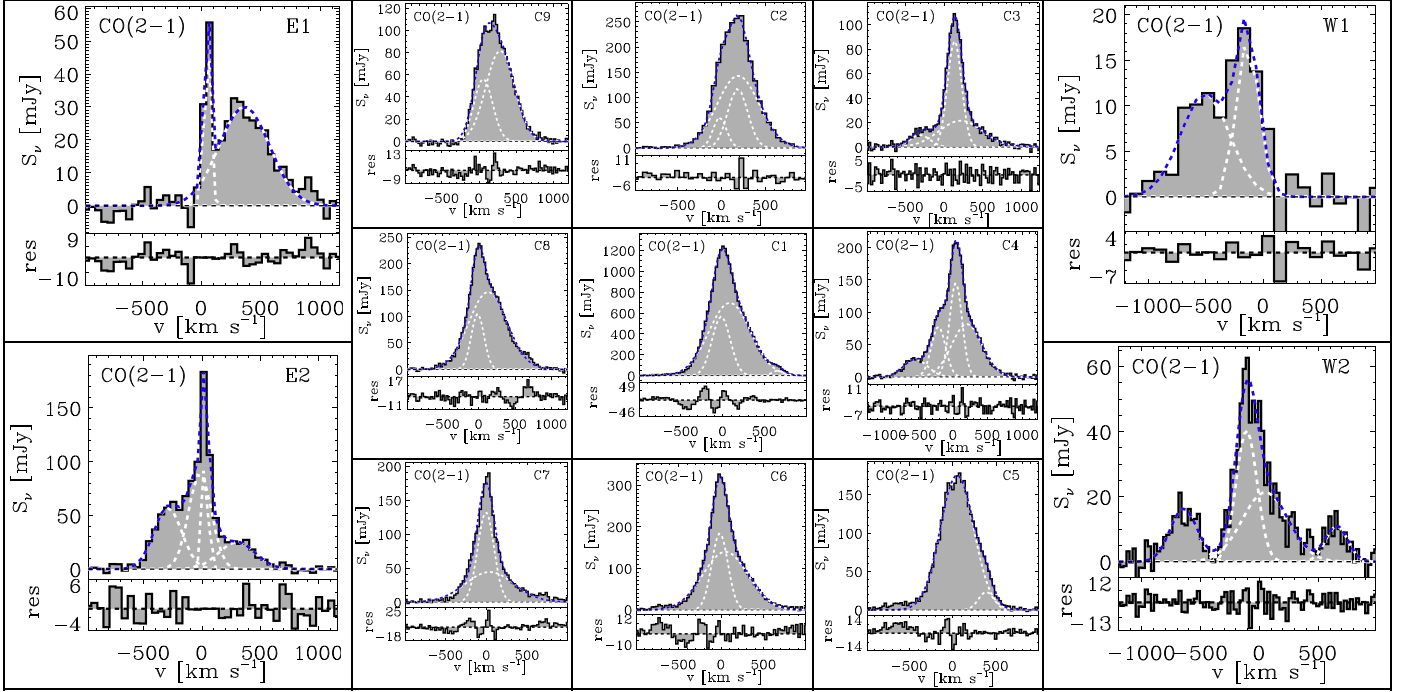
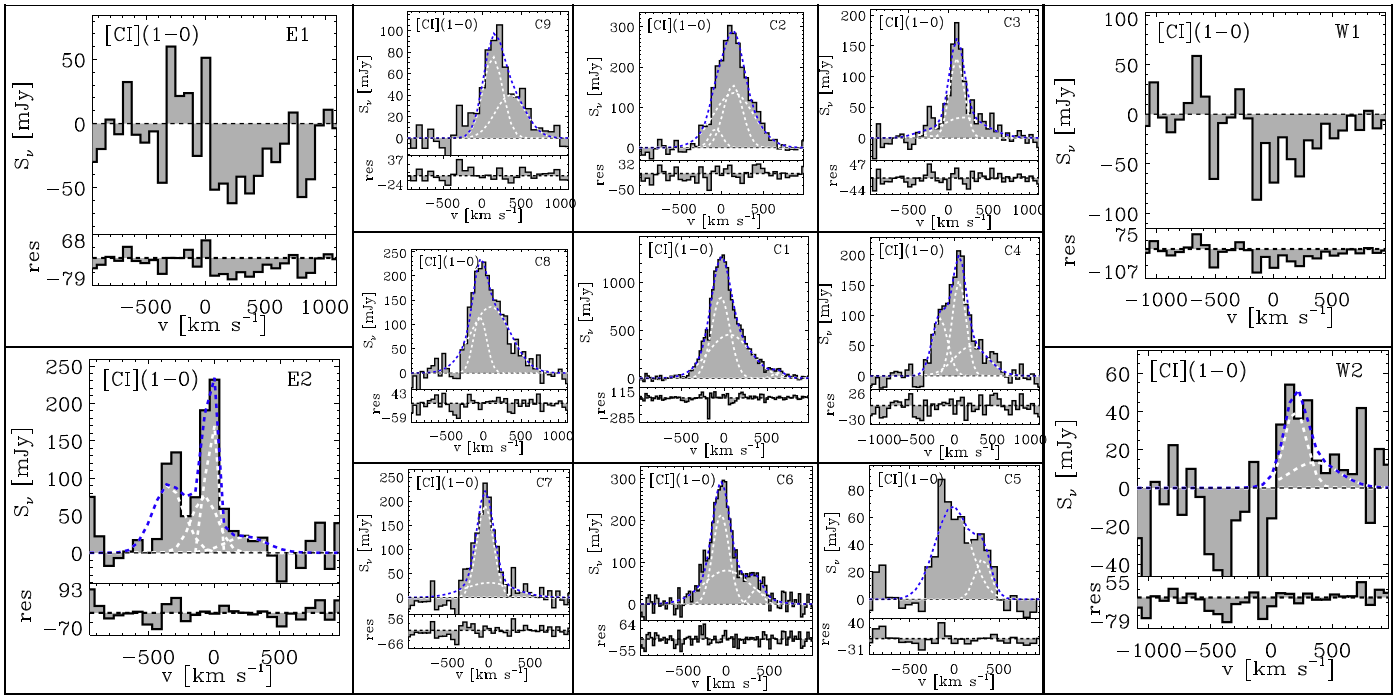


Figure 9. CO(2-1) spectra extracted from the grid of 13 boxes shown in panel (a) of Figure 1, with overplotted the results of the simultaneous fit procedure.



**Figure 10.** [C I](1–0) spectra extracted from the grid of 13 boxes shown in panel (a) of Figure 1, with overplotted the results of the simultaneous fit procedure.

### ORCID iDs

Claudia Cicone <https://orcid.org/0000-0003-0522-6941>  
 Ezequiel Treister <https://orcid.org/0000-0001-7568-6412>  
 George C. Privon <https://orcid.org/0000-0003-3474-1125>  
 Kevin Schawinski <https://orcid.org/0000-0001-5464-0888>

### References

- Aalto, S., Booth, R. S., Black, J. H., & Johansson, L. E. B. 1995, *A&A*, **300**, 369
- Aalto, S., García-Burillo, S., Müller, S., et al. 2012, *A&A*, **537**, A44
- Aalto, S., García-Burillo, S., Müller, S., et al. 2015, *A&A*, **574**, A85
- Alaghband-Zadeh, S., Chapman, S. C., Swinbank, A. M., et al. 2013, *MNRAS*, **435**, 1493
- Alatalo, K., Blitz, L., Young, L. M., et al. 2011, *ApJ*, **735**, 88
- Alatalo, K., Lacy, M., Lanz, L., et al. 2015, *ApJ*, **798**, 31
- Baan, W. A., Hagiwara, Y., & Hofner, P. 2007, *ApJ*, **661**, 173
- Barcos-Muñoz, L., Aalto, S., Thompson, T. A., et al. 2018, *ApJL*, **853**, L28
- Biernacki, P., & Teyssier, R. 2018, *MNRAS*, **475**, 5688
- Bisbas, T. G., Papadopoulos, P. P., & Viti, S. 2015, *ApJ*, **803**, 37
- Bisbas, T. G., van Dishoeck, E. F., Papadopoulos, P. P., et al. 2017, *ApJ*, **839**, 90
- Bolatto, A. D., Wolfire, M., & Leroy, A. K. 2013, *ARA&A*, **51**, 207
- Braine, J., Duc, P.-A., Lisenfeld, U., et al. 2001, *A&A*, **378**, 51
- Brüggen, M., & Scannapieco, E. 2016, *ApJ*, **822**, 31
- Bryant, P. M., & Scoville, N. Z. 1999, *AJ*, **117**, 2632
- Carniani, S., Marconi, A., Maiolino, R., et al. 2015, *A&A*, **580**, A102
- Carniani, S., Marconi, A., Maiolino, R., et al. 2017, *A&A*, **605**, A105
- Cicone, C., Brusa, M., Ramos Almeida, C., et al. 2018, *NatAs*, **2**, 176
- Cicone, C., Feruglio, C., Maiolino, R., et al. 2012, *A&A*, **543**, A99
- Cicone, C., Maiolino, R., Gallerani, S., et al. 2015, *A&A*, **574**, A14
- Cicone, C., Maiolino, R., Sturm, E., et al. 2014, *A&A*, **562**, A21
- Colbert, E. J. M., Wilson, A. S., & Bland-Hawthorn, J. 1994, *ApJ*, **436**, 89
- Combes, F., García-Burillo, S., Casasola, V., et al. 2013, *A&A*, **558**, A124
- Costa, T., Rosdahl, J., Sijacki, D., & Haehnelt, M. G. 2018, *MNRAS*, **473**, A197
- Costa, T., Sijacki, D., & Haehnelt, M. G. 2014, *MNRAS*, **444**, 2355
- Costa, T., Sijacki, D., & Haehnelt, M. G. 2015, *MNRAS*, **448**, L30
- Costagliola, F., Aalto, S., Rodríguez, M. I., et al. 2011, *A&A*, **528**, A30
- Danielson, A. L. R., Swinbank, A. M., Smail, I., et al. 2011, *MNRAS*, **410**, 1687
- Dasyra, K. M., & Combes, F. 2012, *A&A*, **541**, L7
- Dasyra, K. M., Combes, F., Oosterloo, T., et al. 2016, *A&A*, **595**, L7
- Davies, R. I., Maciejewski, W., Hicks, E. K. S., et al. 2014, *ApJ*, **792**, 101
- Downes, D., & Solomon, P. M. 1998, *ApJ*, **507**, 615
- Emonts, B. H. C., Lehnert, M. D., Dannerbauer, H., et al. 2018, *MNRAS*, **477**, L60
- Engel, H., Davies, R. I., Genzel, R., et al. 2010, *A&A*, **524**, A56
- Faucher-Giguère, C.-A., & Quataert, E. 2012, *MNRAS*, **425**, 605
- Feruglio, C., Ferrara, A., Bischetti, M., et al. 2017, *A&A*, **608**, A30
- Feruglio, C., Fiore, F., Maiolino, R., et al. 2013a, *A&A*, **549**, A51
- Feruglio, C., Fiore, F., Piconcelli, E., et al. 2013b, *A&A*, **558**, A87
- Feruglio, C., Maiolino, R., Piconcelli, E., et al. 2010, *A&A*, **518**, L155
- Fiore, F., Feruglio, C., Shankar, F., et al. 2017, *A&A*, **601**, A143
- Fischer, J., Sturm, E., González-Alfonso, E., et al. 2010, *A&A*, **518**, L41
- Fluetsch, A., Maiolino, R., Carniani, S., et al. 2018, *MNRAS*, submitted (arXiv:1805.05352)
- Gallimore, J. F., & Beswick, R. 2004, *AJ*, **127**, 239
- García-Burillo, S., Combes, F., Usero, A., et al. 2014, *A&A*, **567**, A125
- García-Burillo, S., Combes, F., Usero, A., et al. 2015, *A&A*, **580**, A35
- Gaspari, M., & Sądowski, A. 2017, *ApJ*, **837**, 149
- Gerssen, J., van der Marel, R. P., Axon, D., et al. 2004, *AJ*, **127**, 75
- Glover, S. C. O., Clark, P. C., Micic, M., & Molina, F. 2015, *MNRAS*, **448**, 1607
- González-Alfonso, E., Fischer, J., Bruderer, S., et al. 2018, *ApJ*, **857**, 66
- Gowardhan, A., Spoon, H., Riechers, D. A., et al. 2018, *ApJ*, **859**, 35
- Greve, T. R., Papadopoulos, P. P., Gao, Y., & Radford, S. J. E. 2009, *ApJ*, **692**, 1432
- Hacar, A., Tafalla, M., Forbrich, J., et al. 2018, *A&A*, **610**, A77
- Hagiwara, Y., Baan, W. A., & Klöckner, H.-R. 2011, *AJ*, **142**, 17
- Heckman, T. M., Armus, L., & Miley, G. K. 1990, *ApJS*, **74**, 833
- Hopkins, P. F., Quataert, E., & Murray, N. 2012, *MNRAS*, **421**, 3522
- Iono, D., Wilson, C. D., Takakuwa, S., et al. 2007, *ApJ*, **659**, 283
- Ishibashi, W., & Fabian, A. C. 2015, *MNRAS*, **451**, 93
- Israel, F. P., Rosenberg, M. J. F., & van der Werf, P. 2015, *A&A*, **578**, A95
- Jiao, Q., Zhao, Y., Zhu, M., et al. 2017, *ApJL*, **840**, L18
- Keene, J., Blake, G. A., Phillips, T. G., Huggins, P. J., & Beichman, C. A. 1985, *ApJ*, **299**, 967
- Kelly, B. C. 2007, *ApJ*, **665**, 1489
- King, A. R. 2010, *MNRAS*, **402**, 1516
- Krips, M., Martín, S., Sakamoto, K., et al. 2016, *A&A*, **592**, L3
- Lamastra, A., Menci, N., Fiore, F., et al. 2017, *A&A*, **607**, A18



- Leroy, A. K., Walter, F., Bigiel, F., et al. 2009, *AJ*, **137**, 4670
- Leroy, A. K., Walter, F., Martini, P., et al. 2015, *ApJ*, **814**, 83
- Lindberg, J. E., Aalto, S., Muller, S., et al. 2016, *A&A*, **587**, A15
- Maiolino, R., Russell, H. R., Fabian, A. C., et al. 2017, *Natur*, **544**, 202
- Mangum, J. G., & Shirley, Y. L. 2015, *PASP*, **127**, 266
- Max, C. E., Canalizo, G., Macintosh, B. A., et al. 2005, *ApJ*, **621**, 738
- McMullin, J. P., Waters, B., Schiebel, D., Young, W., & Golap, K. 2007, in ASP Conf. Ser. 376, *Astronomical Data Analysis Software and Systems XVI*, ed. R. A. Shaw, F. Hill, & D. J. Bell (San Francisco, CA: ASP), 127
- Meijerink, R., Kristensen, L. E., Weiß, A., et al. 2013, *ApJL*, **762**, L16
- Morganti, R., Frieswijk, W., Oonk, R. J. B., Oosterloo, T., & Tadhunter, C. 2013, *A&A*, **552**, L4
- Morganti, R., Veilleux, S., Oosterloo, T., Teng, S. H., & Rupke, D. 2016, *A&A*, **593**, A30
- Mukherjee, D., Bicknell, G. V., Sutherland, R., & Wagner, A. 2016, *MNRAS*, **461**, 967
- Müller-Sánchez, F., Nevin, R., Comerford, J. M., et al. 2018, *Natur*, **556**, 345
- Nakai, N., Hayashi, M., Handa, T., et al. 1987, *PASJ*, **39**, 685
- Nardini, E., Wang, J., Fabbiano, G., et al. 2013, *ApJ*, **765**, 141
- Nims, J., Quataert, E., & Faucher-Giguère, C.-A. 2015, *MNRAS*, **447**, 3612
- Ojha, R., Stark, A. A., Hsieh, H. H., et al. 2001, *ApJ*, **548**, 253
- Oosterloo, T., Raymond Oonk, J. B., Morganti, R., et al. 2017, *A&A*, **608**, A38
- Papadopoulos, P. P., Bisbas, T. G., & Zhang, Z. 2018, *MNRAS*, **478**, 1716
- Papadopoulos, P. P., & Greve, T. R. 2004, *ApJL*, **615**, L29
- Papadopoulos, P. P., Thi, W.-F., & Viti, S. 2004, *MNRAS*, **351**, 147
- Papadopoulos, P. P., van der Werf, P., Xilouris, E., Isaak, K. G., & Gao, Y. 2012a, *ApJ*, **751**, 10
- Papadopoulos, P. P., van der Werf, P. P., Xilouris, E. M., et al. 2012b, *MNRAS*, **426**, 2601
- Papadopoulos, P. P., Zhang, Z.-Y., Xilouris, E. M., et al. 2014, *ApJ*, **788**, 153
- Pety, J. 2005, in SF2A-2005: Semaine de l'Astrophysique Française, ed. F. Casoli et al. (Paris: EdP-Sciences), 721
- Planck Collaboration, Ade, P. A. R., Aghanim, N., et al. 2016, *A&A*, **594**, A13
- Puccetti, S., Comastri, A., Bauer, F. E., et al. 2016, *A&A*, **585**, A157
- Richings, A. J., & Faucher-Giguère, C.-A. 2018, *MNRAS*, **474**, 3673
- Saito, T., Iono, D., Ueda, J., et al. 2018, *MNRAS*, **475**, L52
- Sakamoto, K., Aalto, S., Combes, F., Evans, A., & Peck, A. 2014, *ApJ*, **797**, 90
- Sakamoto, K., Ho, P. T. P., & Peck, A. B. 2006, *ApJ*, **644**, 862
- Sanders, D. B., Mazzarella, J. M., Kim, D.-C., Surace, J. A., & Soifer, B. T. 2003, *AJ*, **126**, 1607
- Scoville, N., Sheth, K., Aussel, H., et al. 2016, *ApJ*, **820**, 83
- Silk, J., & Rees, M. J. 1998, *A&A*, **331**, L1
- Solomon, P. M., Downes, D., Radford, S. J. E., & Barrett, J. W. 1997, *ApJ*, **478**, 144
- Spoon, H. W. W., Farrah, D., Leboutteiller, V., et al. 2013, *ApJ*, **775**, 127
- Sturm, E., González-Alfonso, E., Veilleux, S., et al. 2011, *ApJL*, **733**, L16
- Tacconi, L. J., Genzel, R., Tecza, M., et al. 1999, *ApJ*, **524**, 732
- Tanaka, K., Oka, T., Matsumura, S., Nagai, M., & Kamegai, K. 2011, *ApJL*, **743**, L39
- Thompson, T. A., Fabian, A. C., Quataert, E., & Murray, N. 2015, *MNRAS*, **449**, 147
- Thompson, T. A., Quataert, E., Zhang, D., & Weinberg, D. H. 2016, *MNRAS*, **455**, 1830
- Turner, B. E. 1985, *ApJ*, **299**, 312
- van der Werf, P. P., Genzel, R., Krabbe, A., et al. 1993, *ApJ*, **405**, 522
- Veilleux, S., Bolatto, A., Tombesi, F., et al. 2017, *ApJ*, **843**, 18
- Veilleux, S., Meléndez, M., Sturm, E., et al. 2013, *ApJ*, **776**, 27
- Veilleux, S., Rupke, D. S. N., Kim, D.-C., et al. 2009, *ApJS*, **182**, 628
- Veilleux, S., Shopbell, P. L., Rupke, D. S., Bland-Hawthorn, J., & Cecil, G. 2003, *AJ*, **126**, 2185
- Walter, F., Bolatto, A. D., Leroy, A. K., et al. 2017, *ApJ*, **835**, 265
- Walter, F., Weiß, A., Downes, D., Decarli, R., & Henkel, C. 2011, *ApJ*, **730**, 18
- Walter, F., Weiss, A., & Scoville, N. 2002, *ApJL*, **580**, L21
- Wang, J., Nardini, E., Fabbiano, G., et al. 2014, *ApJ*, **781**, 55
- Weiß, A., Downes, D., Henkel, C., & Walter, F. 2005, *A&A*, **429**, L25
- Weiß, A., Henkel, C., Downes, D., & Walter, F. 2003, *A&A*, **409**, L41
- Wolfire, M. G., Hollenbach, D., & McKee, C. F. 2010, *ApJ*, **716**, 1191
- Yao, L., Seaquist, E. R., Kuno, N., & Dunne, L. 2003, *ApJ*, **588**, 771
- Yoshida, M., Yagi, M., Ohyama, Y., et al. 2016, *ApJ*, **820**, 48
- Zhang, Z.-Y., Papadopoulos, P. P., Ivison, R. J., et al. 2016, *RSOS*, **3**, 160025
- Zschaechner, L. K., Walter, F., Bolatto, A., et al. 2016, *ApJ*, **832**, 142
- Zubovas, K., & King, A. 2012, *ApJL*, **745**, L34
- Zubovas, K., & King, A. R. 2014, *MNRAS*, **439**, 400